Three-dimensional numerical modeling of temperature and mantle flow fields associated with subduction of the Philippine Sea plate, southwest Japan

Ji, Yingfeng
Yoshioka, Shoichi
Matsumoto, Takumi

(Citation)
Journal of Geophysical Research: Solid,121(6):4458-4482

(Issue Date)
2016-06

(Resource Type)
journal article

(Version)
Version of Record

(URL)
https://hdl.handle.net/20.500.14094/90005033

AGU PUBLICATIONS

JGR

Journal of Geophysical Research: Solid Earth

RESEARCH ARTICLE
10.1002/2016JB012912

Key Points:
- 3-D numerical simulation for thermal regime associated with subduction of the curved PHS plate beneath SW Japan
- Interplate temperature and its gradient affect the distribution of LFEs and SSEs beneath SW Japan
- A new explanation for the aseismic zone of the LFEs beneath eastern Shikoku and the Kii channel

Supporting Information:
- Supporting Information S1

Correspondence to:
Y. Ji,
31911431@qq.com

Citation:
Ji, Y., S. Yoshioka, and T. Matsumoto (2016), Three-dimensional numerical modeling of temperature and mantle flow fields associated with subduction of the Philippine Sea plate, southwest Japan, *J. Geophys. Res. Solid Earth*, *121*, 4458–4482, doi:10.1002/2016JB012912.

Received 11 FEB 2016
Accepted 27 MAY 2016
Accepted article online 1 JUN 2016
Published online 23 JUN 2016

Three-dimensional numerical modeling of temperature and mantle flow fields associated with subduction of the Philippine Sea plate, southwest Japan

Yingfeng Ji[1], Shoichi Yoshioka[1,2], and Takumi Matsumoto[3]

[1]Research Center for Urban Safety and Security, Kobe University, Kobe, Japan, [2]Department of Planetology, Graduate School of Science, Kobe University, Kobe, Japan, [3]National Research Institute for Earth Science and Disaster Prevention, Tsukuba, Japan

Abstract We investigated temperature and mantle flow distributions associated with subduction of the Philippine Sea (PHS) plate beneath southwest Japan, by constructing a three-dimensional parallelepiped model incorporating a past clockwise rotation, the bathymetry of the Philippine Sea plate, and distribution of the subducting velocity within its slab. The geometry of the subducting plate was inferred from contemporary seismic studies and was used as a slab guide integrated with historical plate rotation into the 3-D simulation. Using the model, we estimated a realistic and high-resolution temperature field on the subduction plate interface, which was constrained by a large number of heat flow data, and attempted to clarify its relationship with occurrences of megathrust earthquakes, long-term slow slip events (L-SSEs), and nonvolcanic low-frequency earthquakes (LFEs). Results showed that the oblique subduction coupled with the 3-D geometry of subducting PHS plate was a key factor affecting the interplate and intraplate temperature distributions, leading to a cold anomaly in the plate interface beneath western Shikoku, the Bungo Channel, and the Kii Peninsula. Temperatures in the slab core in these regions at a depth near the continental Moho were nearly 200°C lower than that in eastern Shikoku, indicating a high thermal lateral heterogeneity within the subducting plate. The geothermal control of the LFEs beneath western Shikoku was estimated to be within a range from 400 to 700°C, and the interplate temperature for the L-SSEs with a slip larger than 15 cm beneath the Bungo Channel was estimated to be approximately 350–500°C. A large horizontal temperature gradient of 2.5 ~ °C/km was present where the LFEs occurred repeatedly. The steep temperature change was likely to be related to the metamorphic phase transformation from lawsonite or blueschist to amphibolite of hydrous minerals of the mid-ocean ridge basalt of the subducting PHS plate.

1. Introduction

The northern rim of the Philippine Sea (PHS) plate is subducting beneath the Amurian plate along the Nankai Trough, where megathrust earthquakes such as the *M*8.0-class Tonankai (1944) and Nankai (1946) earthquakes have occurred repeatedly. Through seismic reflection surveys and high-resolution *P* wave seismic tomography studies [e.g., *Nakajima and Hasegawa*, 2007; *Hirose et al.*, 2008; *Nakanishi et al.*, 2012; *Zhao et al.*, 2012], the geometry of the upper surface of the PHS plate beneath southwest Japan has been well estimated (Figure 1). Unlike other planar oceanic plates, the slab geometry in southwest Japan is complex [e.g., *Shiomi et al.*, 2008]. How the interplate thermal state and flow in the upper mantle interact with dehydration in relation to the plate geometry remains an interesting issue to be investigated. Furthermore, the PHS plate is currently obliquely subducting at an azimuth of approximately 30° anticlockwise from the trough-perpendicular direction [*DeMets et al.*, 2010]. Subduction obliquity varies along the curved slab geometry, which poses a challenge for three-dimensional (3-D) numerical simulations with a prescribed geometry and velocity of the subducting oceanic plate. Induced mantle flow in the upper mantle can be obtained as a result of modeling.

Oblique subduction for the curved geometry gives rise to along-arc convection in the upper mantle and heterogeneity of the thermal regime on the plate interface in the along-arc direction. However, it is not clear how the curved slab and oblique subduction influence the thermal regime and arc magmatism and induce small-scale mantle flow in the low viscous mantle wedge. For example, how does the interplate temperature vary along the curved slab and how does the mantle flow between the two bulges of the PHS slab beneath Shikoku and the Kii Peninsula evolve? *Nakajima and Hasegawa* [2007] suggested that the low dip angle could

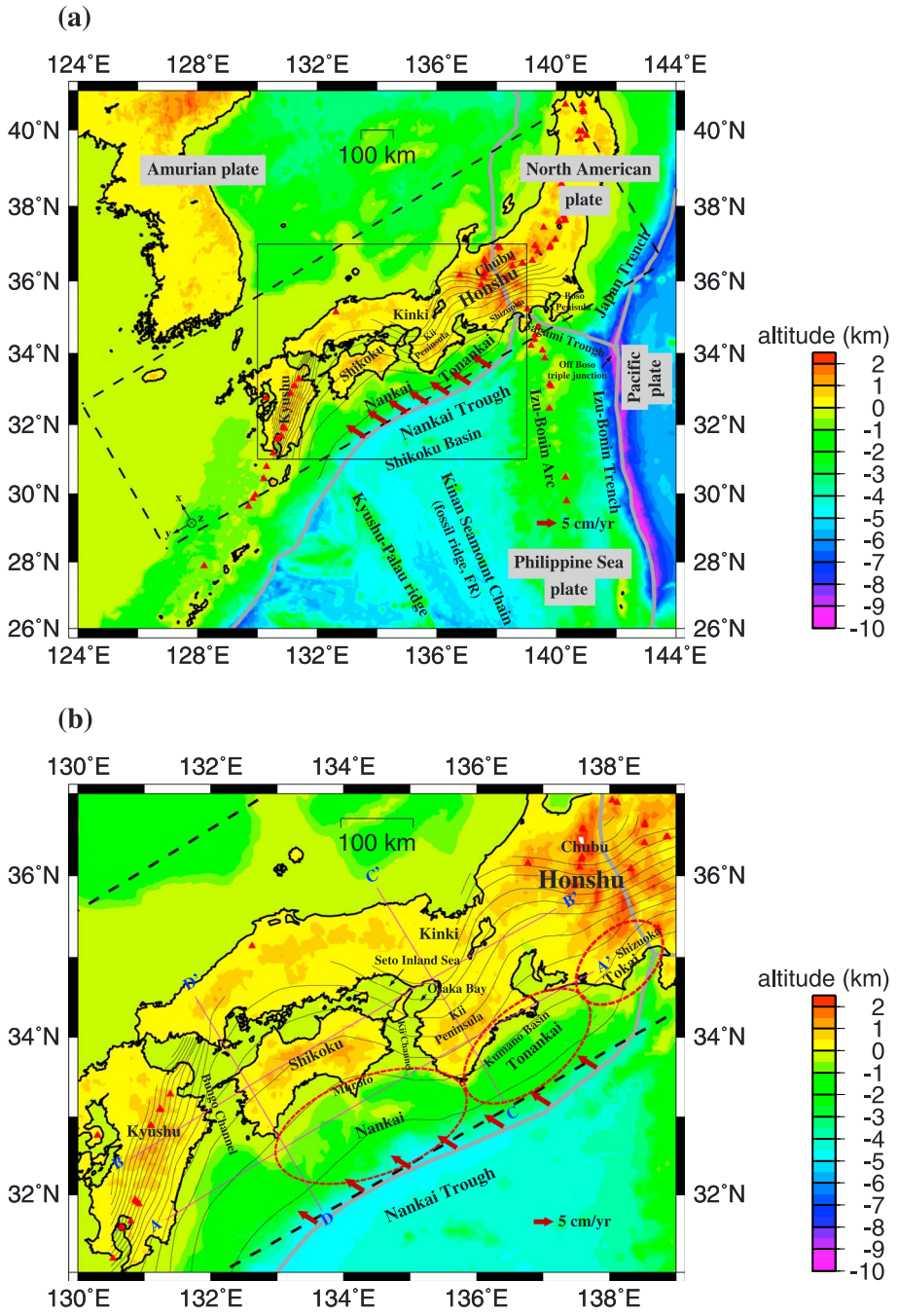

Figure 1. (a) Tectonic map of the southwest Japanese Islands. Colors indicate the altitude. The isodepth contours of the upper surface of the Philippine Sea (PHS) plate, which are drawn with thin black curves, are taken from *Nakajima and Hasegawa* [2007], *Hirose et al.* [2008], and *Nakanishi et al.* [2012]. The gray curves indicate the plate boundaries. The red triangles denote active volcanoes in Japan. The solid red arrows denote plate motion vectors of the PHS plate with respect to the Amurian plate along the Nankai Trough [*DeMets et al.*, 2010]. The dashed black rectangle indicates the modeled region in this study. Orientation of *x-y-z* coordinate axes of the model is marked. (b) Tectonic map of southwest Japan. The solid black rectangle indicates the subduction zone in southwest Japan as zoomed out in Figure 1b. The pink lines A-A′, B-B′, C-C′, and D-D′ indicate the profiles of the temperature distribution and mantle flow field shown in Figures 8a and 8b and 9a and 9b, respectively. The three broken red ellipses denote the imaged source regions of the Tokai, Tonankai, and Nankai great earthquakes as provided by *the Headquarters for Earthquake Research Promotion* [2004].

not induce sufficient mantle upwelling to generate magmas, based on the concentration and absence of volcanoes in the Chubu and Kinki districts, respectively. *Shiomi et al.* [2008] proposed that the interaction between the continental Moho geometry and the plate motion of the subducting PHS plate plays an important role in determining the local stress field, the location of both seismicity and low-frequency earthquakes (LFEs), and the existence of an aseismic slab beneath the central part of Shikoku and the northern part of the Kinki district. *Obara and Hirose* [2006] also found that nonvolcanic deep tremors distribute themselves parallel to the strike of the subducting PHS plate. Their distribution coincides with the depth contours of the plate interface at depths of 35–45 km [*Nakamura et al.*, 1997]. Deep tremors in western Shikoku are more frequent than those in eastern Shikoku and the Kii Channel. The geometry of the oceanic plate also seems to affect their seismicity. The use of 3-D numerical modeling is believed to be an effective way to estimate the thermal regime in the deep tremor zone.

The 3-D numerical simulation of the subduction of an oceanic plate remains one of the most challenging numerical approaches toward the interpretation of geodynamic processes [e.g., *Tackley*, 1998; *Funiciello et al.*, 2003, 2008; *Lassak et al.*, 2006; *Stegman et al.*, 2006, 2010a, 2010b; *Di Giuseppe et al.*, 2008; *Goes et al.*, 2008; *Long and Silver*, 2008; *Ozbench et al.*, 2008; *Schmeling et al.*, 2008; *van Keken et al.*, 2008; *Capitanio et al.*, 2009; *Morra et al.*, 2009; *Wada and Wang*, 2009; *Jadamec and Billen*, 2010; *Zhu et al.*, 2010; *Capitanio and Morra*, 2012; *Li and Ribe*, 2012; *Manea et al.*, 2012; *Strak and Schellart*, 2014]. In recent decades, several issues regarding thermomechanical models have been highlighted by numerous studies, including the lateral variation of the subduction process in 3-D [e.g., *Tackley*, 2000; *Honda and Saito*, 2003; *Morra et al.*, 2006; *Schellart et al.*, 2007]. *Gerya* [2011] reported that two tendencies currently exist in subduction model design, including kinematically prescribed models and more dynamic models, with the latter being difficult to apply to specific subduction zones if the rheology of a plate is not sufficiently well known [*Honda*, 2008; *Morishige et al.*, 2010; *Yoshida et al.*, 2012]. *Tackley and Xie* [2003] presented the 3-D thermal convection model "stag3D" that spontaneously generates plates through treatment of the strong viscosity variations, solid-solid phase changes, and compositional differentiation.

However, modeling the shallower interplate thermal state with complex slab geometry has received less attention so far. The latest developments in 3-D kinematic modeling include models of prescribed geometry and velocity [*Kneller and van Keken*, 2008], a moving plate boundary [*Honda*, 2008], a 3-D time-dependent kinematic-dynamic model to investigate the along-margin thermal structure between the Japan and Kurile arcs [*Morishige and van Keken*, 2014], and a 3-D thermal model with a realistic 3-D slab geometry in northeast Japan to investigate the mantle wedge flow pattern [*Wada et al.*, 2015]. *Yoshioka and Murakami* [2007] proposed that the temperature distribution on the plate interface of the subducting PHS plate beneath southwest Japan is diversified beneath a continental plate. *Kneller and van Keken* [2008] revealed that convex and concave slab geometries caused lower or higher pressure at the same depth by 3-D numerical modeling, respectively. *Völker et al.* [2011] suggested a thermal control on the seismogenic zone in southern central Chile, based on a 2-D finite element modeling. They suggested that the downdip limit of the shallow cluster of seismicity corresponds to 325°C on the modeled temperature field along some profiles. *Ji and Yoshioka* [2015] investigated the relationships among dip angle, subduction obliquity, and the interplate thermal regime by several models for theoretically constructed convex and concave slabs.

In this study, we constructed a 3-D thermal convection model with arbitrary slab geometry developed from stag3D [*Tackley and Xie*, 2003] to describe the heterogeneity of the thermal regime on the plate interface as well as its relationship with the interplate seismic events. To avoid confusion between the terms "dip angle" and "subduction angle" in this study, we refer to subduction angle as the dip angle of an oceanic plate along the direction of its oblique subduction, whereas dip angle refers to along the trough-perpendicular direction.

2. Methodology

2.1. Governing Equations

In this study, we employed anelatic liquid approximation and used the equations of conservation of mass, momentum, and energy [e.g., *Yoshioka and Murakami*, 2007]. The equation of conservation of mass is given by

$$\frac{\partial[\rho_s(z,T_s)v_i]}{\partial x_i}=0, \tag{1}$$

Table 1. Values of Model Parameters for Numerical Simulations of Subduction of the Three-Dimensionally Curved PHS Plate

Symbol	Parameters	Value	Units
ρ_0	Standard density	3300[a]	kg/m^3
T_0	Temperature difference between top and bottom of model	1600	K
κ_0	Standard thermal conductivity	2.9[b]	w/mK
Hr	Radioactive heat generation rate in the mantle	2.245×10^{-13}[a]	w/m^3
C_{p_0}	Standard specific heat at constant pressure	1200[a]	J/kgK
k_0	Standard thermal diffusivity	7.6×10^{-7}[c]	m^2/s
η_0	Standard viscosity	1×10^{20}[b]	Pa · s
α_0	Standard thermal expansion	3×10^{-5}[d]	/K
v	Oblique subduction velocity	6.0[e]	cm/yr
A	Parameters to calculate the interplate shear stress	6.12×10^{-2}[f]	Mpa^{-n}
m	Parameters to calculate the interplate shear stress	3.05[f]	1
Q	Parameters to calculate the interplate shear stress	2.76×10^{2}[f]	kJ/mol

[a] *Wang et al.* [1995].
[b] *Christensen* [1996].
[c] *Yoshioka and Murakami* [2007].
[d] *Iwamori* [1997].
[e] *DeMets et al.* [2010].
[f] *Caristan* [1982].

where the 3-D Cartesian coordinates (x, y, z) are represented by (x_1, x_2, x_3). Parameter $\rho_s(z, T_s)$ is the density at depth z and temperature T_s, and v_i is the ith component of the flow velocity vector $\mathbf{v}$. The suffix s denotes adiabatic condition. The momentum equation can be expressed as

$$-\frac{\partial P}{\partial x_i}+\frac{\partial \tau_{ij}}{\partial x_j}-\Delta_{i3}\rho_s g\alpha_0(T-T_s)=0, \tag{2}$$

where P is the pressure deviation from hydrostatic pressure, τ_{ij} is a stress tensor, Δ_{ij} is Kronecher's Delta, g is gravitational acceleration, and α_0 is the reference thermal expansivity. T_s can be written by

$$\frac{dT_s}{dx_3}=\frac{g\alpha_0}{C_{p_0}}T_s, \tag{3}$$

where C_{p0} is the specific heat at constant pressure.

The density ρ depends on temperature

$$\rho=\rho_s(z,T_s)[1-\alpha_0(T-T_s)]. \tag{4}$$

The energy equation can be expressed by

$$\rho C_{p0}\left(\frac{\partial T}{\partial t}+\mathbf{v}\cdot\nabla T\right)=k\nabla^2T+\tau_{ij}\dot{\varepsilon}_{ij}+\rho g\alpha_0 Tv_3+\rho H_r+\rho C_{p0}v_e(x,y)\frac{\partial T}{\partial z}, \tag{5}$$

where k is the thermal conductivity, η is the viscosity, $\dot{\varepsilon}_{ij}$ is the strain rate tensor, v_3 is the flow velocity component in the vertical direction, H_r is the internal radioactive heating per unit mass, and $v_e(x, y)$ is the vertical rate of surface erosion and sedimentation in the upper continental crust at a surface coordinate (x, y). The left-hand side of the equation includes the advection term $\rho C_{p0}\mathbf{v}\cdot\nabla T$. On the right-hand side, a thermal diffusion term $k\nabla^2T$, viscous dissipation term $\tau_{ij}\dot{\varepsilon}_{ij}$ for the viscous upper mantle and the solid-solid subduction interface, adiabatic heating term $\rho g\alpha_0 Tv_3$, and radioactive heating term ρH_r are included. Viscous dissipation inside the slab was assumed to be zero, for the subduction velocity was prescribed there. The dissipation item on the solid-solid subduction interface can be simplified as a frictional heating term $\tau_s\dot{\varepsilon}_s$, where τ_s is the frictional stress and $\dot{\varepsilon}_s$ is the shear strain rate. H_r is the internal heating per unit mass. According to *Furukawa* [1999], *Fukahata and Matsu'ura* [2000], and *Yoshioka et al.* [2013], the frictional heating term on a plate interface $\tau_s\dot{\varepsilon}_s$ and the temperature change term $\rho C_{p0}v_e(x,y)\frac{\partial T}{\partial z}$ due to the effect of surface erosion and sedimentation rates during the Quaternary period are also taken into account in the energy equation. The related model parameters are tabulated in Table 1.

2.2. Viscous Flow Law

For viscosity η, we followed the viscous flow law for wet olivine from *Burkett and Billen* [2010]. Laboratory experiments indicate that the deformation of olivine occurs by both diffusion creep ($_{df}$) and dislocation creep

Table 2. Model Parameters for Wet Olivine at Constant Water Content [*Hirth and Kohlstedt*, 2003; *Burkett and Billen*, 2010]

		Flow Law Parameters	
	Parameter	Diffusion Creep	Dislocation Creep
n_0	Stress exponent	1.0	3.5
A_0	Preexponential factor ($s^{-n}Pa^{-n}\,\mu m^{p}H^{-r}\,10^{6r}\,Si^{r}$)	1.0	9.0×10^{-20}
E_0	Activiation energy (kJ/mol)	335	480
V_0	Activation volume (m^3/mol)		
	Upper mantle	4.0×10^{-6}	11.0×10^{-6}
	Lower mantle	1.5×10^{-6}	-
d	Grain size(μm)		
	Upper mantle	10,000	-
	Lower mantle	40,000	-
p	Grain size exponent	3.0	-
C_{OH}	OH concentration (H/10^6Si)	1,000	1,000
r	C_{OH} exponent	1.0	1.2

($_{ds}$) in the upper mantle, where each mechanism accommodates a portion of the total strain rate [*Hirth and Kohlstedt*, 2003]

$$\dot{\varepsilon}_t = \dot{\varepsilon}_{\mathrm{df}} + \dot{\varepsilon}_{\mathrm{ds}}. \tag{6}$$

The composite upper mantle viscosity for deformation at constant stress is given by

$$\eta_{\mathrm{comp}} = \frac{\eta_{\mathrm{df}}\eta_{\mathrm{ds}}}{\eta_{\mathrm{df}} + \eta_{\mathrm{ds}}}, \tag{7}$$

where η_{df} and η_{ds} are the diffusion creep and dislocation creep viscosities for olivine, respectively. The general form of the viscosity law is

$$\eta_{\mathrm{df,ds}} = \left(\frac{d^p}{A_0 C_{OH}^r}\right)^{\frac{1}{n}} \dot{\varepsilon}_E^{\frac{1-n}{n}} \exp\left(\frac{E_0 + P_l V_0}{n_0 R T_a}\right), \tag{8}$$

where $\dot{\varepsilon}_E = \left(\frac{1}{2}\dot{\varepsilon}_{ij}\dot{\varepsilon}_{ij}\right)^{\frac{1}{2}}$ is given by the square root of the second invariant of the strain rate tensor [*Ranalli*, 1995], T_a is the absolute temperature, R is the gas constant, and P_l is the lithostatic pressure defined by a compressibility gradient in the mantle

$$P_l = -\frac{1}{\beta_a}\ln(1 - \rho_0 g \beta_a z), \tag{9}$$

where z is depth, ρ_0 is the standard density, and the adiabatic compressibility $\beta_a = 4.3\times10^{-12}\,\mathrm{Pa}^{-1}$ [*Turcotte and Schubert*, 2002]. The values of the model parameters for diffusion and dislocation creep of olivine used in this study such as n_0, A_0, E_0, V_0, d, p, C_{OH}, and r are tabulated in Table 2.

2.3. Frictional Heating on a Plate Interface

The frictional heating term on a plate interface $\tau_s\dot{\varepsilon}_s$ is dependent on the pore pressure ratio λ. Referring to *Wang et al.* [1995] and *Yoshioka et al.* [2013], we incorporated frictional heating on the plate interface associated with plate subduction into our model. Deformation style under a brittle regime differs remarkably from that under a ductile regime on the plate interface. In the former case, shear stress at a plate boundary has a linear relation with the normal stress σ_n at each depth. Following *Byerlee* [1978], the relation is expressed as

$$\tau_s = 0.85\sigma_n(1-\lambda) \quad [\sigma_n(1-\lambda) \le 200MPa], \tag{10}$$

$$\tau_s = 50 + 0.6\sigma_n(1-\lambda) \quad [\sigma_n(1-\lambda \ge 200MPa]. \tag{11}$$

The parameter of the pore pressure ratio λ is a key parameter used to determine the magnitude of frictional heating on the plate interface. λ is defined as [*Wang et al.*, 1995]

$$\lambda = \frac{P_f - P_d}{P_l - P_d}, \tag{12}$$

where P_f is pore pressure, P_d is the pressure at the Earth's surface, and P_l is lithostatic pressure. Since $P_f \le P_l$ and $P_d \le P_f$, $0 \le \lambda \le 1$, considering the various possibilities for the real conditions of the pore pressure ratio on the plate interface, we assigned different values of 0.98 – 1.0 [*Seno*, 2009; *Yoshioka et al.*, 2015b] for λ.

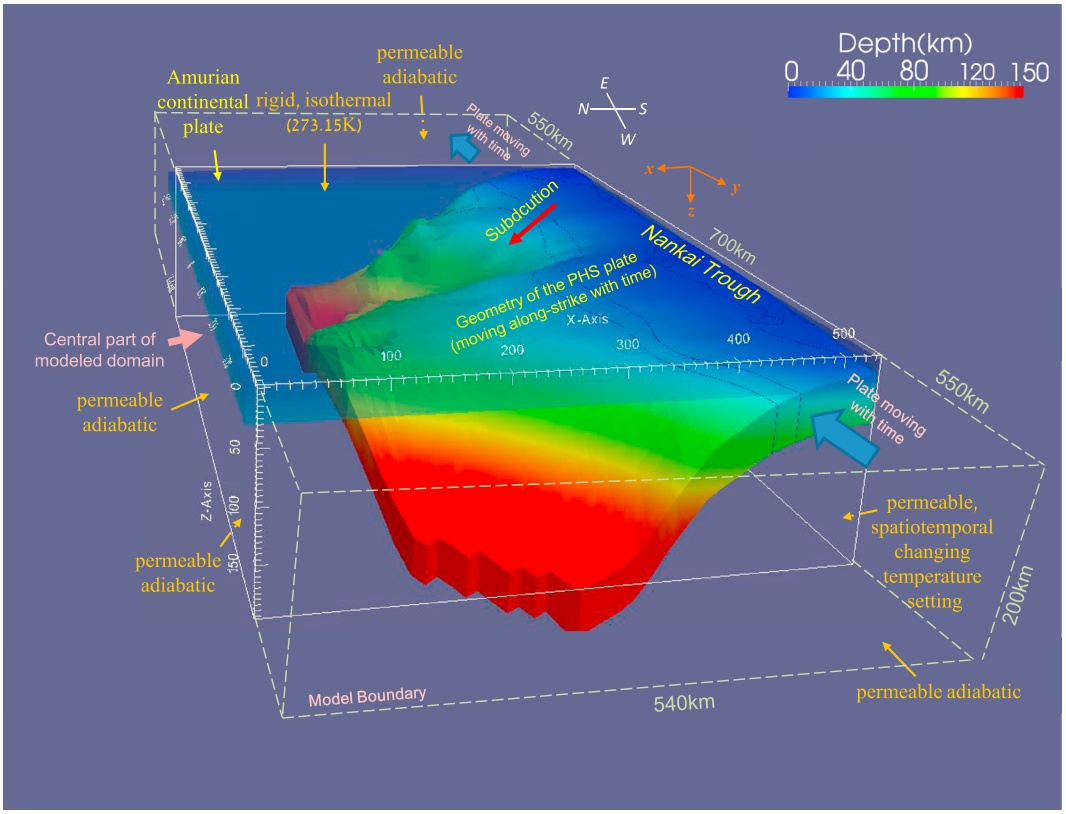

Figure 2. A three-dimensional (3-D) model of the subducting PHS plate and its boundary conditions. The right-upper rim coincides with the Nankai Trough.

At depths greater than the diabase curve [*Caristan*, 1982], the substances on the plate interface transform from a brittle to ductile regime. For a ductile regime, shear stress has an exponential relation with strain rate, which is represented by the ratio of the subduction velocity v_d and the thickness of the interplate deforming layer w (assumed to be 500 m), referring to *Caristan* [1982] and *Wang et al.* [1995]

$$\tau_s = \frac{1}{2} A^{-\frac{1}{m}} \dot{\varepsilon}^{\frac{1}{m}} \exp\left(\frac{Q}{mRT}\right), \tag{13}$$

A, m, and Q are experimentally determined parameters with values given by *Caristan* [1982] and tabulated in Table 1. In both regimes, we assume

$$\dot{\varepsilon}_s = \frac{v_d}{w}, \tag{14}$$

where τ_s indicates the shear stress at the plate interface and $\dot{\varepsilon}_s$ is the shear strain rate.

2.4. Erosion and Sedimentation Rates During the Quaternary Period

With regard to the effects of surface erosion and sedimentation rates on the temperature field, according to *Fukahata and Matsu'ura* [2000] and *Yoshioka et al.* [2013], the continent has witnessed a period of notable uplift and subsidence for the last 2 Myr during the Quaternary period [*the Research Group for the Quaternary Tectonic Map*, 1969]. The uplifted land surface has slowly been eroded away with erosion scraping away the thickness of the continental crust and simultaneously increasing the surface heat flow. Conversely, where sedimentation has occurred, the crust has thickened and surface heat flow has decreased. These effects of erosion and sedimentation, hereafter referred to as EES, on thermal structure are represented by $\rho C_{p0} v_e(x) \frac{\partial T}{\partial z}$ in the energy equation for 2-D modeling [*Fukahata and Matsu'ura*, 2000; *Yoshioka et al.*, 2013]. In 3-D simulation, the average land uplift rate (mm/yr) was obtained by *Yoshikawa* [1974] as

$$v_e(x,y) = 2\times10^{-6} U_q(x,y) - 0.37, \tag{15}$$

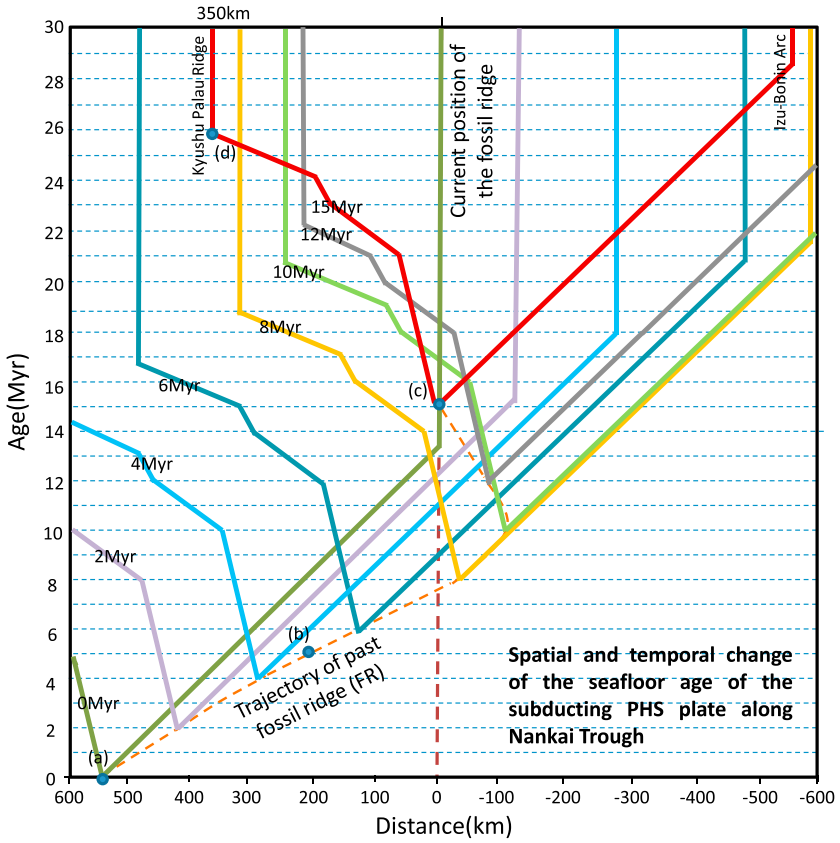

Figure 3. Spatiotemporal plot of the seafloor age of the subducting PHS plate along Nankai Trough. The age was inferred from the shade relief map of magnetic anomalies [*Okino et al.*, 1999] and referred to the subduction history of the PHS plate [*Mahony et al.*, 2011; *Clift et al.*, 2013]. The dashed yellow curve indicates the trajectory of past ridge axis. The variable slopes of quasi-linear V-shaped lines near the FR (fossil ridge) for different periods were obtained based on the past spreading rates of the Shikoku Basin. The west of the Kyushu-Palau ridge (50 Ma~) [*Tokuyama*, 1995] and the eastern part of the PHS plate, including the Izu-Bonin Arc (40 Ma~) [*Nakajima and Hasegawa*, 2007], were also included in the model. The four blue circles denote the following: (a) The FR of the PHS plate at 15 Ma was located 500–600 km southwest of its current position at the Nankai Trough. (b) It was located 200 km southwest at 10 Ma. (c) The age of the current FR is 15 Myr. (d) The current seafloor at the eastern rim of the Kyushu-Palau ridge is approximately 350 km west of the ridge.

where $U_q(x, y)$ is the amount (mm) of uplift and subsidence at the surface coordinate (x, y) during the Quaternary period. We calculated $v_e(x, y)$ and evaluated the EES distribution in southwest Japan for the last 2 Myr during the Quaternary period.

3. Model

3.1. Geometry, Thickness, and Velocity of the Subducting Plate

Referring to *Nakajima and Hasegawa* [2007], *Hirose et al.* [2008], *Nakanishi et al.* [2012], and *Zhao et al.* [2012], we obtained the geometry of the upper surface of the PHS plate. The best fit 3-D geometry of the PHS plate was constructed, using the interpolation and extrapolation of these data (Figure 2).

Considering that the slab is becoming thicker over time, we used the following equation as a derivation from *Yoshii* [1975] to calculate the thickness of the PHS plate (km) within which the subduction velocity is prescribed:

$$d_{\mathrm{ocea}} = c_v t_{\mathrm{ocea}}{}^{\frac{1}{2}} = 7.5 t_{\mathrm{ocea}}{}^{\frac{1}{2}}, \tag{16}$$

where t_{ocea}(Myr) is the age of the PHS plate along the Nankai Trough, which is given in Figure 3. C_v was assumed to be 7.5 $\left(\mathrm{km\ Myr}^{-\frac{1}{2}}\right)$, following *Yoshii* [1975].

In the model, the along-arc direction parallel to the Nankai Trough is assumed to be the *y* axis, the direction normal to the Nankai Trough is assumed to be the *x* axis, and the vertical downward direction is the *z*axis (Figure 2).

Coordinates x, y, and z are the distances from the trough axis and the centermost edge, and the depth from the model surface, respectively. Since the location of the PHS plate shifted in association with rotation from 15 to 3 Ma, we first set the domain of the slab, which is represented by the prescribed guide, at each time step. Next, we calculated the subduction angle of the PHS plate at every time step and for every grid, by taking the depth difference and distance between two neighboring grids. For boundary grids without enough neighboring grids, we performed a linear interpolation or extrapolation. The subduction velocities inside the prescribed guide of the geometry of the PHS plate were given by [*Ji and Yoshioka*, 2015]

$$v_{dx} = \begin{cases} \left\{a(x,y)^2 + 1 + 2a(x,y)b(x,y)\tan\theta + \left[b(x,y)^2 + 1\right]\tan^2\theta\right\}^{-\frac{1}{2}} v_d, |\theta| < 90°, \\ 0, |\theta| = 90° \end{cases} \tag{17}$$

$$v_{dy} = \begin{cases} v_{dx}\tan\theta, |\theta| < 90° \\ \left[b(x,y)^2 + 1\right]^{-\frac{1}{2}} v_d, |\theta| = 90° \end{cases}, \tag{18}$$

$$v_{dz} = \begin{cases} a(x,y)v_{dx} + b(x,y)v_{dy}, |\theta| < 90° \\ b(x,y)v_{dy}, |\theta| = 90° \end{cases}, \tag{19}$$

with

$$a(x,y) = \frac{1}{2}\{Z(x+\Delta x, y) - Z(x-\Delta x, y)\}\cdot\frac{z_{\max}}{x_{\max}}, \tag{20}$$

$$b(x,y) = \frac{1}{2}\{Z(x+\Delta x, y+\Delta y) - Z(x+\Delta x, y) + Z(x-\Delta x, y) - Z(x-\Delta x, y-\Delta y)\}\cdot\frac{z_{\max}}{y_{\max}}, \tag{21}$$

where θ is the horizontal azimuth of plate subduction from the north counter clockwise. Parameters $x_{\max}$, $y_{\max}$, and $z_{\max}$ are the dimensions of the parallelepiped model ($x_{\max}$ = 540 km, $y_{\max}$ = 1800 km, and $z_{\max}$ = 200 km). Parameter v_d is the subducting velocity of the oceanic plate, and v_{dx}, v_{dy}, and v_{dz} are the velocity components of v_d in the $+x$, $+y$, and $+z$ directions, respectively. $Z(x,y)$ is the depth of the upper surface of the slab at grid (x,y). Parameters Δx and Δy are the grid intervals between two neighboring grids along the x and y axes, respectively. The grid intervals are 10 km in length (Δx), 15 km in width (Δy), and 5 km in depth (Δz). The temperature for the entire model domain and the mantle flow outside the prescribed oceanic slab were solved throughout the numerical simulation.

3.2. Initial and Boundary Conditions

The initial temperature condition of the whole model region is given by

$$T = T_0 \mathrm{erf}\left(\frac{z}{2\sqrt{\frac{k_0 t_{\mathrm{cont}}}{\rho_0 C_{p0}}}}\right), \tag{22}$$

with

$$t_{\mathrm{cont}} = \left(\frac{d_{\mathrm{cont}}}{C_v}\right)^2, \tag{23}$$

where t_{cont} and d_{cont} are the age (Myr) and an assigned apparent thickness (km) of the continental crust, respectively. The thermal regime under the continental crust is affected by d_{cont}. By fitting the calculated heat flow to the observed heat flow, we estimated the most appropriate value of d_{cont} using a trial-and-error method as described later.

The mantle flow and temperature conditions of the model boundary are imposed by a rigid and isothermal (0°C) upper surface ($-z$), permeable and adiabatic bottom ($+z$), left side ($+y$), right side ($-y$), and front side ($+x$) (Figure 2). The continental crust with a thickness of 32 km is assumed to be conductive. The boundary temperature condition at the back side ($-x$), that is beneath the Nankai Trough, will be explained in a later section. Flow velocities inside the slab were imposed by equations (17)–(21).

The oceanic PHS plate was prescribed to subduct from the Nankai Trough ($-x$ side) into the parallelepiped model domain with a slab geometry moving along-arc with time when it was rotating during the period from

Table 3. The PHS Plate Rotation and Subduction Assumed in This Study

Period	Plate Motion of the PHS Plate	Plate Motion Velocity (cm/yr)	Azimuth (Clockwise From the North)
15 Ma–13 Ma	Oblique subduction	7.5	−30.8°
13 Ma–11 Ma	Transition to pure rotation	7.5	−30.8°–60°
11 Ma–7 Ma	Rotation	7.5	60°
7 Ma–4 Ma	Transition to oblique subduction	7.5	60° to −55.4°
4 Ma–3 Ma	Oblique subduction	5.43	−55.4°
3 Ma–0 Ma	Oblique subduction (MORVEL)	6.0	−58.8°

15 to 3 Ma and held fixed with materials inside the prescribed guide extending downward when the guide stopped rotation from 3 to 0 Ma.

3.3. Subduction History of the PHS Plate

The cooling age of the PHS plate, taking account of its spreading rate [e.g., *Okino et al.*, 1999] and the change in subduction direction, was considered in the numerical simulation, by imposing a boundary temperature and a scenario with a spatiotemporal changing subduction velocity of the PHS plate. The opening of the Japan Sea is considered to have occurred from 17 to 12 Ma [*Kimura et al.*, 2005]. Following *Wang et al.* [1995] and *Okino et al.* [1999], we assumed that the PHS plate initiated subduction from approximately 15 Ma. The thermal structure of the PHS slab was designed by prescribing a slab that gradually aged and thickened away from the Kinan Seamount Chain, which is hereafter referred to as FR (fossil ridge) (Figure 1a). *Mahony et al.* [2011] and *Clift et al.* [2013] reconstructed tectonics in southwest Japan with evolving relative plate motions shifting northeastward off the Boso triple junction connecting the Japan Trench, the Izu-Bonin Trench, and the Sagami Trough. They suggested that the PHS plate rotated relative to the Eurasian plate during the period from 15 to 5 Ma, which was strongly supported by magmatic and volcano-tectonic studies [*Mahony et al.*, 2011]. With respect to the age of the Kurotaki unconformity near the Boso Peninsula, central Japan, *Takahashi* [2006] proposed that the location of the Euler pole of the PHS plate changed at 3 Ma from east of the triple junction to northeast of Hokkaido. *Yoshioka and Murakami* [2007] suggested that the change was partly caused by the separation of the Amurian (AM) plate from the Eurasian (EU) plate and assumed that the PHS plate was subducting beneath the EU plate rather than the AM plate before the separation. Bathymetric data indicate that the FR trended ~30° counterclockwise from the north. The current plate motion of the PHS plate with respect to the AM plate has been determined using GPS data to be nearly 6.3 cm/yr along the Nankai Trough [*Sella et al.*, 2002]. *Yoshioka and Murakami* [2007] also suggested that the subduction velocity increased from 4.0 cm/yr to the present rate after the separation of the two continental plates.

Taking account of these studies, we assumed that the PHS plate rotated from 15 to 3 Ma with a subduction velocity of approximately 7.5 cm/yr, and then it subducted by approximately 6.0 cm/yr from 3 Ma to the present at nearly N60°W, which is the current convergent velocity and direction obtained by the MORVEL [*DeMets et al.*, 2010] and NNR-MORVEL56 [*Argus et al.*, 2011] models (Table 3). The southern rim of the modeled region coincides with the Nankai Trough where the PHS plate is currently subducting at a velocity of around 6.0 cm/yr [e.g., *DeMets et al.*, 2010].

Figure 2 shows the boundary conditions and 3-D geometry of the subducting PHS plate. Although the current subduction velocity varies along the Nankai Trough, the deviation has remained with less than 1.0 cm/yr [*Sella et al.*, 2002]. Therefore, we used the average value of 6.0 cm/yr to represent the current plate motion with respect to the Amurian plate in our model. For the historical plate convergence, *Mahony et al.* [2011] claimed a subduction velocity of 7–8 cm/yr for the PHS plate from 15 to 5 Ma and a reduction to a velocity of 5–6 cm/yr from 5 to 2 Ma. Hence, we adopted an average subduction velocity of 7.5 cm/yr during the period from 15 to 3 Ma with a rotating direction or an oblique subduction azimuth (Table 3). *Honda and Yoshida* [2005] prescribed a moving plate boundary along the across-arc direction to investigate small-scale convection based on stag3D, which was similar to the approach used in this study. However, the prescribed guide for the PHS plate in this study was set to move in the along-arc direction with plate subduction beneath the continental plate. It is difficult for us to determine all the necessary geophysical properties of the subduction zone to construct a full dynamic subduction model, especially at depths shallower than 50 km to

perfectly fit the slab geometry. Therefore, we took the currently known geometry of the PHS plate to imagine its shape in the past, using the prescribed guide. For the purpose of constructing such a semidynamic model of plate subduction, we followed *Mahony et al.* [2011] and *Clift et al.* [2013] to mimic the historical trench-parallel shift of the PHS plate. The shift of the prescribed guide of the PHS plate lasted from 15 to 3 Ma, after which the guide was fixed spatially with the PHS plate still subducting within the guide. The subduction velocities were imposed within the guide, and the length of the slab gradually increased with calculation time.

To accommodate the trough-parallel shift of the PHS plate, we enlarged the size of the x dimension to 1800 km (see Figure 1a and section 3.1), which is necessary to treat larger-scale trough-parallel motion of the PHS plate (Figure 1b). We discuss in detail the thermal properties on the upper surface of the PHS plate in this central part where Shikoku and the Kii Peninsula are located.

The spatiotemporal change in the age of the seafloor of the PHS plate along the Nankai Trough as a function of its normal distance from the present FR is shown in Figure 3, taking account of the subduction history proposed by *Mahony et al.* [2011] and *Clift et al.* [2013] and the seafloor age obtained from magnetic anomalies [*Okino et al.*, 1999]. The current seafloor age from FR to the Kyushu-Palau ridge ranged from 15 to 26 Myr according to *Okino et al.* [1999]. We also estimated the age of the eastern part of the seafloor at the Nankai Trough to be approximately 15–21 Ma within a distance range from 0 to 250 km away from FR (Figure 3). The west of the Kyushu-Palau ridge (50 Ma~) [*Tokuyama*, 1995] and the eastern part of the PHS plate, including the Izu-Bonin Arc (40 Ma~) [*Nakajima and Hasegawa*, 2007], are considered to be older than the Shikoku Basin, which were also included in the model.

3.4. Spatiotemporal Changing Temperature Boundary Condition Beneath the Nankai Trough

In our model, the evolution of the thermal structure in the vertical cross section at the Nankai Trough followed the model GDH1 to predict the seafloor heat flow [*Stein and Stein*, 1992; *McKenzie*, 1967; *Grose and Afonso*, 2013] with a lithospheric basal temperature T_m

$$T(z, t_{oc}) = T_m \left[\frac{z}{d_0} + \frac{2}{\pi} \sum_{n=1}^{\infty} \frac{1}{n} \sin\left(\frac{n\pi z}{d_0}\right) \exp\left(\frac{-n^2\pi^2\kappa t_{oc}}{{d_0}^2}\right) \right], \tag{24}$$

where $T(z, t_{oc})$ is the temperature at depth z and age t_{oc} of the oceanic plate along the Nankai Trough, d_0 is the depth below which adiabatic heating is applied, and κ is the thermal diffusivity. We calculated the thermal regime at depths on the vertical cross section beneath the Nankai Trough at each time step, by considering the different ages of the PHS plate along the trough. This enables us to impose more realistic spatiotemporal changing thermal boundary conditions to the 3-D thermal model.

4. Results

4.1. Fitting of Calculated Surface Heat Flow to the Observation

We searched for the optimum parameters in the model as a whole to fit the observation of surface heat flow data. *Hamamoto et al.* [2011] calculated the shallow thermal structure off the Kumano Basin, southwest Japan, using a 2-D thermal model for various values of frictional heating on the plate interface and radioactive heat generation rate in the accretionary prism. We selected the parameters with relatively large effects in the model, which were the pore pressure ratio λ, apparent thickness of the continental crust d_{cont}, radioactive heat generation in the upper continental crust Rh_c, and radioactive heat generation in the accretionary prism Rh_a. Among them, λ and d_{cont} were anticorrelated, and Rh_c and Rh_a were correlated with the surface heat flow. In this study, seven models using the different model parameters were constructed, as tabulated in Table 4.

Following a comparison of all the seven models with various model parameter values related to radioactive generation rate and continental age, most models produce similar calculated surface heat flow at the Nankai Trough, except that there are some differences in the profiles b–i of Figures 4 and 5 if comparing Models 2–7 with Model 1 (Figures S1–S6 in the supporting information). We used the least squares of the misfit to evaluate models to find the least variance between the calculation and the observation within the region (x = 0–350 km, y = -350–350 km). In northern Kyushu and the Kii Peninsula, the effects of volcanoes and radioactive elements were excluded for the evaluation. A higher surface heat flow was observed due to the influence of volcanic magma or aggregation of radioactive elements beneath the Kii Peninsula

Table 4. Values of Model Parameters Used in the Modeling

Model	λ	d_{cont} (km)	Rh_c (10^{-10}W/kg)	Rh_a (10^{-10}W/kg)	Remark
1	1.0	32	7.3	0	Standard
2	1.0	35	7.3	0	Larger apparent thickness of the continental crust
3	1.0	40	7.3	0	Larger apparent thickness of the continental crust
4	1.0	32	8.0	0	Higher radioactive heat generation in the upper crust
5	0.98	32	7.3	0	Smaller pore pressure ratio
6	0.99	32	7.3	0	Smaller pore pressure ratio
7	1.0	32	7.3	7.3	Higher radioactive heat generation in the accretionary prism

[*Uehara et al.*, 2003]. Among the seven models, Model 1 (Table 4) was found to fit the observed heat flow best. The results for Model 1 along profiles in the x and y directions are shown in Figures 4 and 5, respectively. We took eight profiles in the x direction in southwest Japan, being perpendicular to the Nankai Trough from profiles $y = -105$ to 105 km (Figure 4), and parallel to the Nankai Trough from profiles $x = 15$ to 225 km (Figure 5). In these figures, the observed and calculated heat flow distributions along these profiles are plotted within a width of 30 km in the x and y directions, respectively. In terms of either the long or short wavelength variation of the calculated heat flow, the calculated results were considered to be consistent well with the observation.

4.2. Sensitivity of Model Parameters Influencing the Surface Heat Flow

Comparing Model 1, which is the best fit model, with the other models, we found that a larger thickness of the continental plate d_{cont} (a larger plate age t_{cont}) was in effect equivalent to a smaller thermal conductivity for the continental plate and had an impact on the surface heat transport. For example, at a depth of 50 km below the continent, the temperature decreased by more than 50°C when d_{cont} changed from 32 km ($t_{cont} = 18.2$ Myr) to 40 km ($t_{cont} = 28.4$ Myr). A larger d_{cont} also contributed to a lower surface heat flow in the continental crust, where the average heat flow was reduced by approximately 10–15 mW/m^2 (approximately 1–2 mW/m^2 for every 1 km increase in d_{cont}). Hence, d_{cont} was one of the most sensitive parameters affecting the crustal heat flow in the modeled region of southwest Japan. In contrast, d_{ocea} only affected the continental plate near the convergence zone, where the oceanic plate is shallow enough to transport the cold temperature of the oceanic plate to the Earth's surface. Every 1 km increase in d_{ocea} resulted in a decrease of ~1 mW/m^2 when the subduction angle of the subducting plate was roughly 10°. The radioactive generation rate Rh_c and Rh_a changed the value of heat flow by approximately 3–5 mW/m^2 when we changed the value of either Rh_c or Rh_a by 10% of the standard value of 7.3×10^{-10} W/m^3. Their impact on heat flow was similar to that of d_{cont}, but weaker than that of λ whose effect will be discussed in detail in the next section. For the interplate temperature, d_{cont} had a more significant role than Rh_c. Similarly, the age of the slab and the subduction velocity were also important factors having an impact on the interplate temperature and the surface heat flow when the oceanic plate subducted for long periods and was shallow enough beneath the studied regions. In short, the parameters d_{cont} and Rh_c covered a broader region in the continental plate than the parameters λ and Rh_a, which mainly covered the fore arc and accretionary prism, respectively.

Because the four key parameters as well as some others are not well known, if the values of d_{cont} and λ are changed at the same time, there will probably be another optimum model with parameter pairs (d_{cont}, λ) that fit the observations well. This is due to the nonuniqueness of the solutions and inadequate understanding of the real geophysical constraints. It should be noted that the optimum solution in our model was one of the optimum solution sets. We also recognized that most of the model parameters are spatially variable, and their spatial distributions have to be determined as much as possible to obtain a more realistic model, which is beyond the scope of this study.

4.3. Effect of Erosion/Sedimentation and Interplate Frictional Heating on Surface Heat Flow

In this study, uplift and subsidence rates on land were assumed to occur only during the Quaternary period in the last 2 Myr. The effect of erosion and sedimentation rates on the upper crust is distinguishable mainly in terrestrial zones in Figures 4a and 5a such as Honshu, the Kii Peninsula, Kyushu, and Shikoku, resulting in an additional short wavelength fluctuation in the calculated surface heat flow on the order of ~30 mW/m^2 in

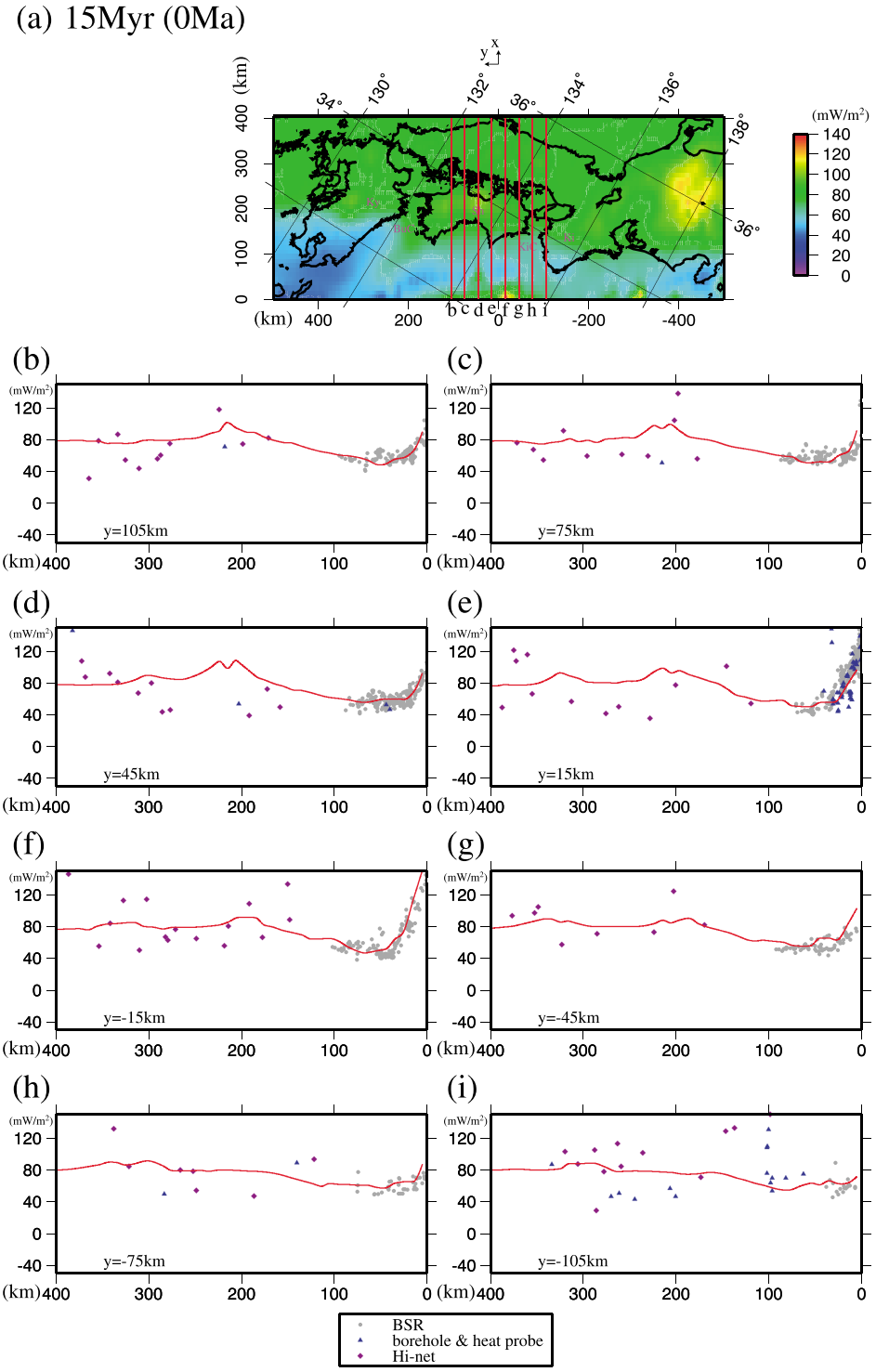

Figure 4. (a) Spatial distribution of the calculated heat flow at 0 Ma for Model 1. Ky: Kyushu, BuC: Bungo Channel, Sh: Shikoku, KiC: Kii Channel, Ki: Kii Peninsula. (b) Observed and calculated heat flows along profile b ($y = 105$ km) in Figure 4a in the x direction. The gray solid circle, blue triangle, and purple diamond denote heat flow data from bottom-simulating reflectors (BSRs) [*Ashi et al.*, 1999, 2002], land boreholes and marine heat probes [*Tanaka et al.*, 2004], and Hi-net boreholes [*Matsumoto*, 2007], respectively, within a width of 30 km. The red curve is the calculated heat flow. (c) Same as Figure 4b but along profile c ($y = 75$ km). (d) Same as Figure 4b but along profile d ($y = 45$ km). (e) Same as Figure 4b but along profile e ($y = 15$ km). (f) Same as Figure 4b but along profile f ($y = -15$ km). (g) Same as Figure 4b but along profile g ($y = -45$ km). (h) Same as Figure 4b but along profile h ($y = -75$ km). (i) Same as Figure 4b but along profile i ($y = -105$ km). The observed and calculated heat flows are compared along the across-arc profiles b to i in Figures 4b to 4i, respectively.

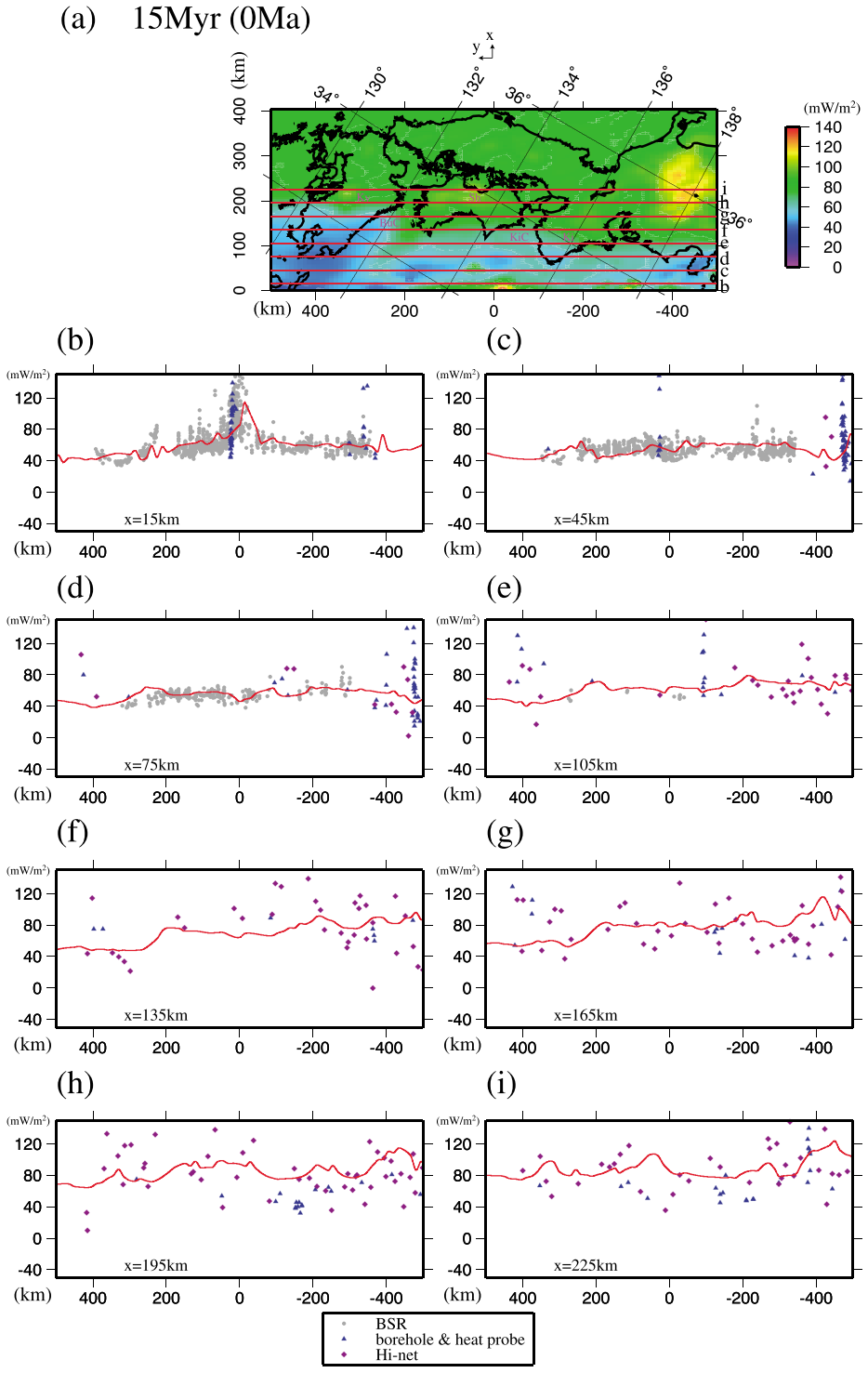

Figure 5. (a) Spatial distribution of the calculated heat flow at 0 Ma for Model 1. Ky: Kyushu, BuC: Bungo Channel, Sh: Shikoku, KiC: Kii Channel, Ki: Kii Peninsula. (b) Observed and calculated heat flows along profile b ($x = 15.0$ km) in Figure 5a in the y direction. The gray solid circle, blue triangle, and purple diamond denote heat flow data from BSRs [*Ashi et al.*, 1999, 2002], land boreholes and marine heat probes [*Tanaka et al.*, 2004], and Hi-net boreholes [*Matsumoto*, 2007], respectively. The red curve is the calculated heat flow within a width of 30 km. (c) Same as Figure 5b but along profile c ($x = 45$ km). (d) Same as Figure 5b but along profile d ($x = 75$ km). (e) Same as Figure 5b but along profile e ($x = 105$ km). (f) Same as Figure 5b but along profile f ($x = 135$ km). (g) Same as Figure 5b but along profile g ($x = 165$ km). (h) Same as Figure 5b but along profile h ($x = 195$ km). (i) Same as Figure 5b but along profile I ($x = 225$ km). The observed and calculated heat flows are compared along the along-arc profiles b to i in Figures 5b to 5i, respectively.

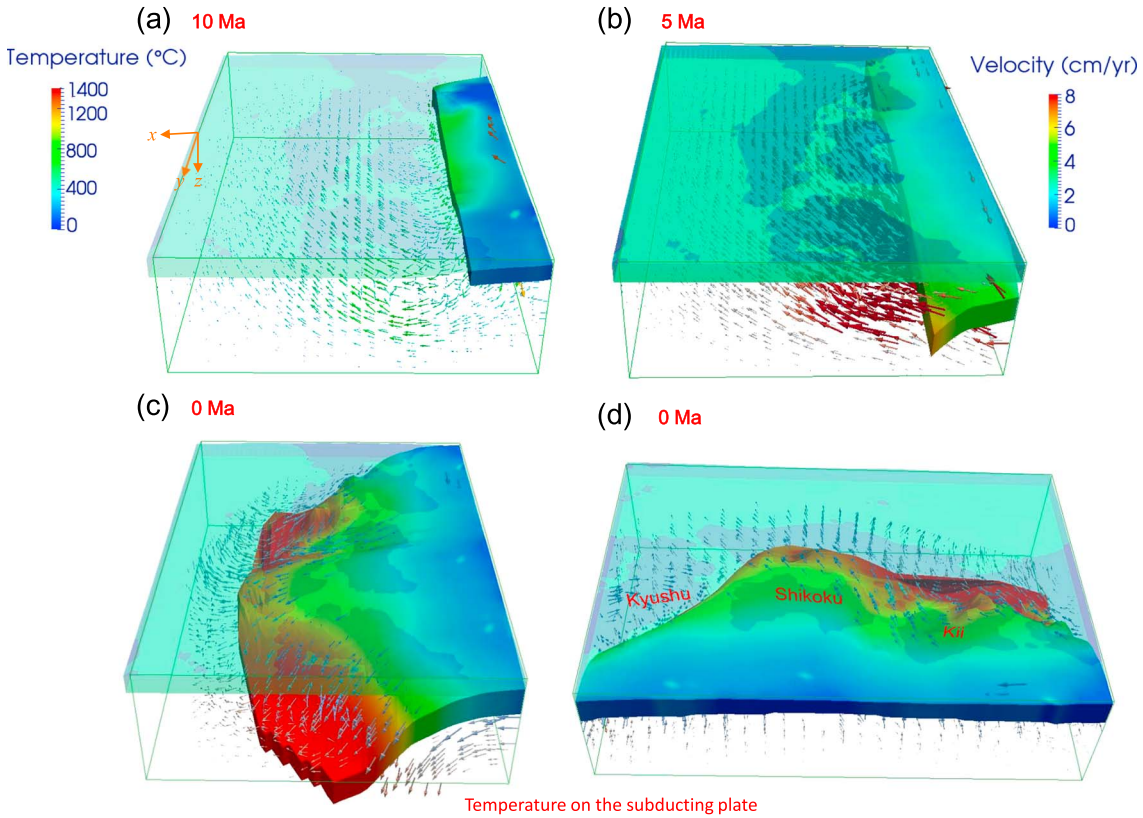

Figure 6. Bird's eye view of the distributions of 3-D mantle flow (color arrows) and slab surface temperature (color) associated with subduction of the PHS plate for Model 1. (a) View from the west at 10 Ma. (b) View from the west at 5 Ma. (c) View from the west at 0 Ma. (d) View from the south at 0 Ma. Kii: Kii Peninsula.

southwest Japan. A positive heat flow anomaly was caused by erosion, corresponding to the land uplift, whereas a negative heat flow anomaly resulting from sedimentation was less distinguishable, which was partly due to the water area such as the inland sea in southwest Japan.

To determine the relationship between interplate frictional heating and surface heat flow, we assigned different values to the pore pressure ratio λ, which is equivalent in effect to the frictional coefficient μ [e.g., *Gao and Wang*, 2014], incorporating them into the model, and performed a sensitivity test. We assumed that $\lambda = 0.95$, 0.98, and 1.00 in Models 5, 6, and 1, respectively. When $\lambda = 0.98$, which was equivalent to $\mu = 0.017$, the crustal heat flow caused by the frictional heating in the Nankai and Tonankai regions increased and exceeded the heat flow observations from BSRs and marine heat probes, which gave an average of 60 mW/m^2 near the Nankai Trough. Some of the calculated heat flow values even reached 100 mW/m^2. Frictional heating increased the surface heat flow, while the sediment and basement relief with a low thermal conductivity was likely to decrease the surface heat flow. Considering the trade off, the calculated value of ~150 mW/m^2 at the FR of the Nankai Trough was still possible, although the observed peak surface heat flow was ~110 mW/m^2 [*Hamamoto et al.*, 2011] and a value of λ of 0.95– (μ = ~0.043) was acceptable. In our study, we assumed the thickness of the frictional layer on the upper surface of the slab to be 0.5 km to calculate the shear strain on the interface of the subduction fault [e.g., *Wang et al.*, 1995]. However, this value was uncertain and variable along with the slab interface. If the thickness of the frictional layer was larger than 0.5 km, the calculated frictional heating would be less than the value calculated in the current models. More importantly, the hydrothermal circulation around the slab interface and endothermic process in serpentinization and dehydration on the plate interface were not considered in our thermal convection models. Therefore, due to the uncertainties of the details of interplate friction, the range of λ values (0.95–1.00) was considered to be acceptable in these models, enabling a possible explanation for the observation to be made. Under the premise of an interplate frictional layer (wet granite) thickness of 0.5 km [*Hansen and Carter*, 1983; *Gao and Wang*, 2014] in our models, a larger pore pressure ratio such as λ being close to 1.00 (μ is smaller) would be preferable to explain the heat flow observation.

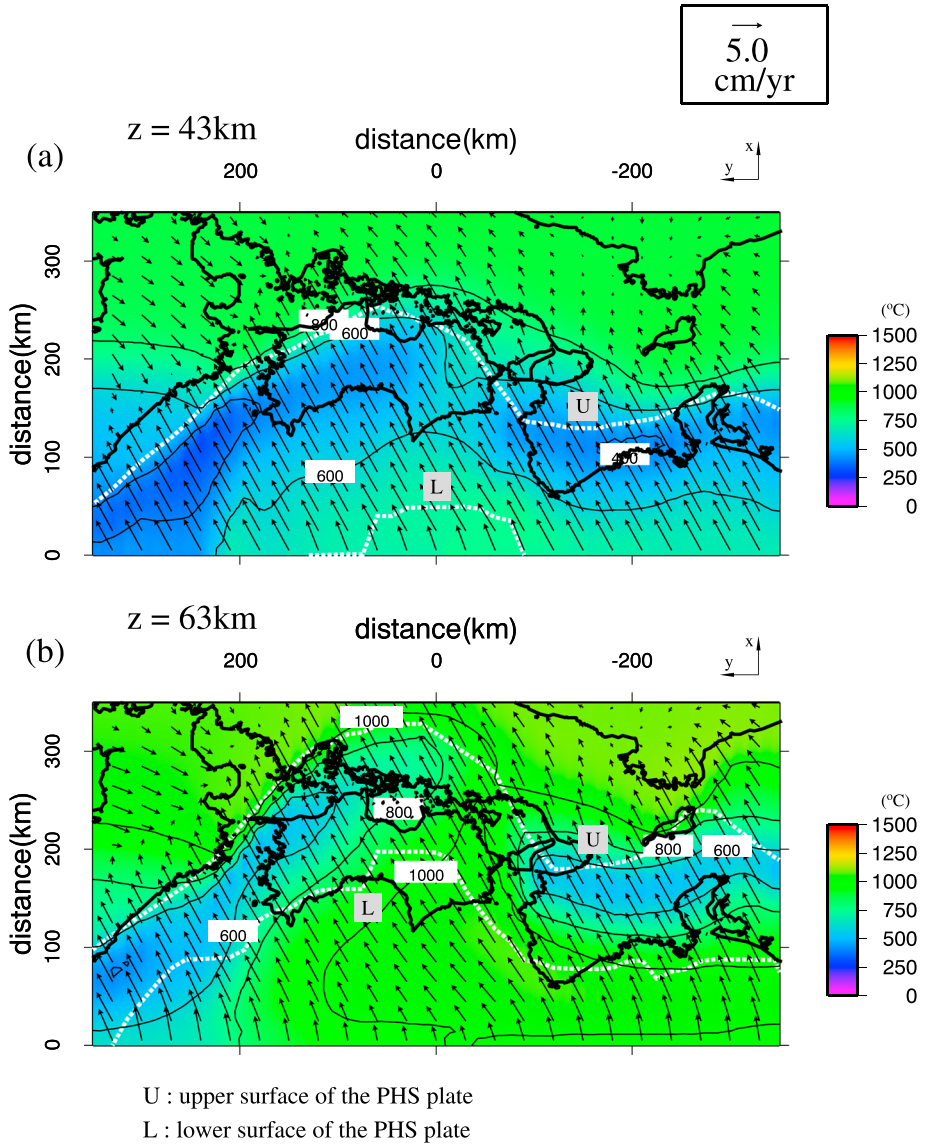

Figure 7. Distributions of temperature (color) and horizontal component of mantle flow (black arrows) at 0 Ma for Model 1. The two white dotted curves indicate the upper and lower surfaces of the subducting PHS plate. (a) A depth of 43 km. (b) A depth of 63 km.

4.4. Thermal Regime and Mantle Flow Associated With Subduction of the PHS Plate

Figures 6a–6c show how the thermal and flow velocity fields developed in the Model 1 at 10, 5, and 0 Ma, respectively. The color contours denote temperatures on the subducting PHS plate, and the arrows represent mantle flows driven by subduction of the plate. The interplate thermal regime evolved corresponding to evolution of the geometry of the PHS plate. We observed that the present upper surface of the PHS plate was relatively shallow beneath Shikoku, which resulted in a cool plate interface beneath the two regions currently (Figure 6d). The highly curved PHS plate with oblique subduction beneath southwest Japan was considered to account for the heterogeneity of the interplate thermal regime on the upper surface of the PHS plate identified in this study.

Furthermore, the induced mantle flows yielded more easily above a steeply subducting plate than a gently subducting plate. For example, the mantle flow atop the plate interface beneath Kyushu was more distinct than that beneath Shikoku and the Kii Peninsula. From 3 Ma, oblique subduction occurred at 6.3 cm/yr, and the mantle flowed near the slab. For the convex bulges of the PHS plate situated beneath Shikoku

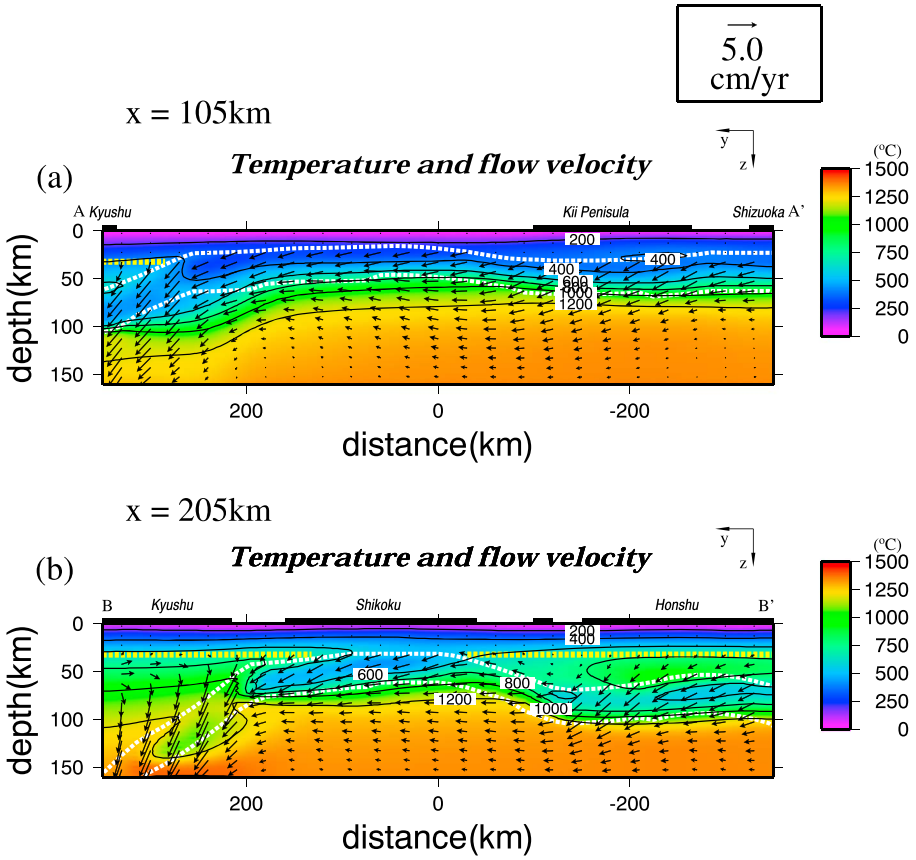

Figure 8. Distributions of temperature (color) and *y-z* component of mantle flow (black arrows) in the *y-z* (trough parallel) vertical cross section at 0 Ma for Model 1. The two white dotted curves indicate the upper and lower surfaces of the subducting PHS plate. The yellow dotted line indicates the continental Moho discontinuity. (a) $x = 105$ km. (b) $x = 205$ km.

and the Kii Peninsula, the induced mantle flow above the slab was weak due to the shallow subduction angle. For example, at the concave part of the PHS plate, such as beneath the Kii Channel and Osaka Bay (Figure 1b), convection in the mantle wedge occurred (Figures 6c and 6d). With regard to the slab geometry, convection in the mantle wedge tends to develop more above a concave geometry than a convex one, for a concave geometry having a larger subduction angle, which was previously documented to be one of the thermal parameters of a subducting oceanic plate [*Gorbatov and Kostoglodov*, 1997].

For closer comparison, we investigated distributions of temperature and mantle flow in the *x-y*, *y-z*, and *x-z* cross sections and plate interface for Model 1, as shown in Figures 7–10, respectively.

Figures 7a and 7b show the temperature distributions at depths of 43 and 63 km, respectively. The results indicated that low-temperature domains exist beneath southwest Japan, and the cooling effect in the domains of Kyushu, the western Shikoku, and the Kii Channel were larger than those on the eastern side of each region. These results are consistent with the hypothesis that lower temperature appears in the slab with a larger subduction angle [e.g., *Ji and Yoshioka*, 2015]. In Figure 7a, at a depth of 43 km, we found that a horizontal temperature difference of nearly 300°C existed inside the PHS slab enclosed by white dotted lines. The subduction angle was ~10° in eastern Shikoku and the Kii Channel, whereas it was nearly 30° approximately in the offshore region of Kyushu. The coldest part was situated beneath southeast Kyushu, and the warmest part was beneath eastern Shikoku. In Figure 7b, at a depth of 63 km, the slab shifts northwestward, still with the warmest part in northeast Shikoku, and with a horizontal temperature difference reaching nearly 500°C inside of the PHS plate. This reveals the lateral inhomogeneity of the inner slab temperature, which significantly impacts on mineral dehydration and pore fluid pressure near the plate interface and inside the subducting oceanic plate. The phase transitions of minerals inside the PHS plate at

depths of 40–60 km have to be re-evaluated, taking the thermal inhomogeneity caused by the 3-D geometry of the slab and oblique subduction into account.

Figure 8 shows the along-arc vertical cross sections of distributions of the temperature and mantle flow in and around the subducting PHS plate (A-A′ and B-B′ of Figure 1b). A sharper bending of the PHS plate occurs beneath Kyushu and the Kii Peninsula than beneath Shikoku. The effect of oblique subduction along a convex plate surface leads to a subduction angle of almost 0° beneath eastern Shikoku and the Kii Channel. Such a small subduction angle may explain why a hot thermal anomaly occurs beneath eastern Shikoku at a depth of 50 km (Figure 8b).

In Figure 9, we also delineated the across-arc vertical cross sections of the thermal regime and mantle flow passing through the eastern Kii Peninsula ($y = -150$ km, C-C′ of Figure 1b) and western Shikoku ($y = 150$ km, D-D′ of Figure 1b), where cold anomalies inside the slab were identified, as shown in Figure 7, proving that the subduction angle in Figure 9a differed from that in Figure 9b. Figure 10 shows the interplate thermal regime in southwest Japan where the temperature contours of 150°C, 350°C, and 450°C and the seismicity distribution are drawn.

5. Discussion

5.1. Influence of Seafloor, Slab Age, and Other Factors on the Calculated Surface Heat Flow

The calculated surface heat flow showed a good fit to the observation of a fluctuation in the short wavelength except for the observed sharp anomaly near the FR of the PHS plate (Figure 5b). The calculated short wavelength is mainly caused by changing vertical distance from the seafloor to the uppermost calculating grid. That is, the upper surface of the model with a temperature of 0°C was prescribed with a depth according to the bathymetry. The introduction of seafloor topography into the 3-D simulation brought the calculated values closer to the observations of the surface heat flow of the BSRs and marine heat probes, especially at the profiles parallel and close to the Nankai Trough. This indicates that the seafloor topography has an important influence on seafloor surface heat flow. If we neglected the seafloor topography in the calculation of surface heat flow, although the general trend with long wavelength features in the calculation was explainable, it was difficult to explain the short wavelength fluctuation along the profiles passing through the seafloor. The calculated heat flow near the FR along the Nankai Trough also deviated from the observed high heat flow under flat top model geometry. Measurements of marine heat flow are commonly performed near the ocean bottom. Thus, we relocated the surface of our model from 0 km to the depth of the regional seafloor (0 km to approximately 5 km), which is assumed to be 0°C to ensure a more accurate calculation for surface heat flow in the ocean. The form of heat flow variation was more consistent with the calculation when the bathymetry correction was made, except near the FR, where a larger anomaly of nearly 30 mW/m^2 still remained. This could be interpreted as an effect of hydrothermal circulation in the aquifer of the subducting PHS plate [*Spinelli and Wang*, 2008; *Harris et al.*, 2013], which would cause a sharp peak in heat flow anomaly near the ridge.

Spinelli and Wang [2008] and *Harris et al.* [2013] reported that fluid circulation accounted for the observed heat flow peak at the Muroto Transect near the FR of the Nankai Trough and the subsequent rapid descent in surface heat flow along the landward profile. *Spinelli and Wang* [2008] also found that the permeability structure of the slab has a large impact on the simulated heat flow along the décollement, and therefore used a different permeability for the FR and the seaward Nankai Trough of the Kii Peninsula and Shikoku. For the sharp landward drop in surface heat flow from the Nankai Trough (Figure 4), we noticed that the seafloor where the peak heat flow occurs at the FR was nearly 4.8 km in depth, which is almost the deepest point of the PHS plate along the Nankai Trough. At 50 km landward from the Nankai Trough, the depth of the seafloor is approximately 3.0 km, with a significant elevation in altitude of approximately 1.8 km, which causes a temperature drop of almost 100°C in the calculation as compared with the FR at the Nankai Trough. The temperature drop at the seafloor affects the calculated surface heat flow of ~100 Wm^{-1} K^{-1}. The rapid landward drop of the surface heat flow is explainable if the effect of seafloor topography and also the hydrothermal circulation are taken into account.

Another possible interpretation for the difference between calculated and observed heat flows is that the sediment (thickness 200–600 m) and basement relief (600–1200 m) on the incoming PHS plate [*Harris*

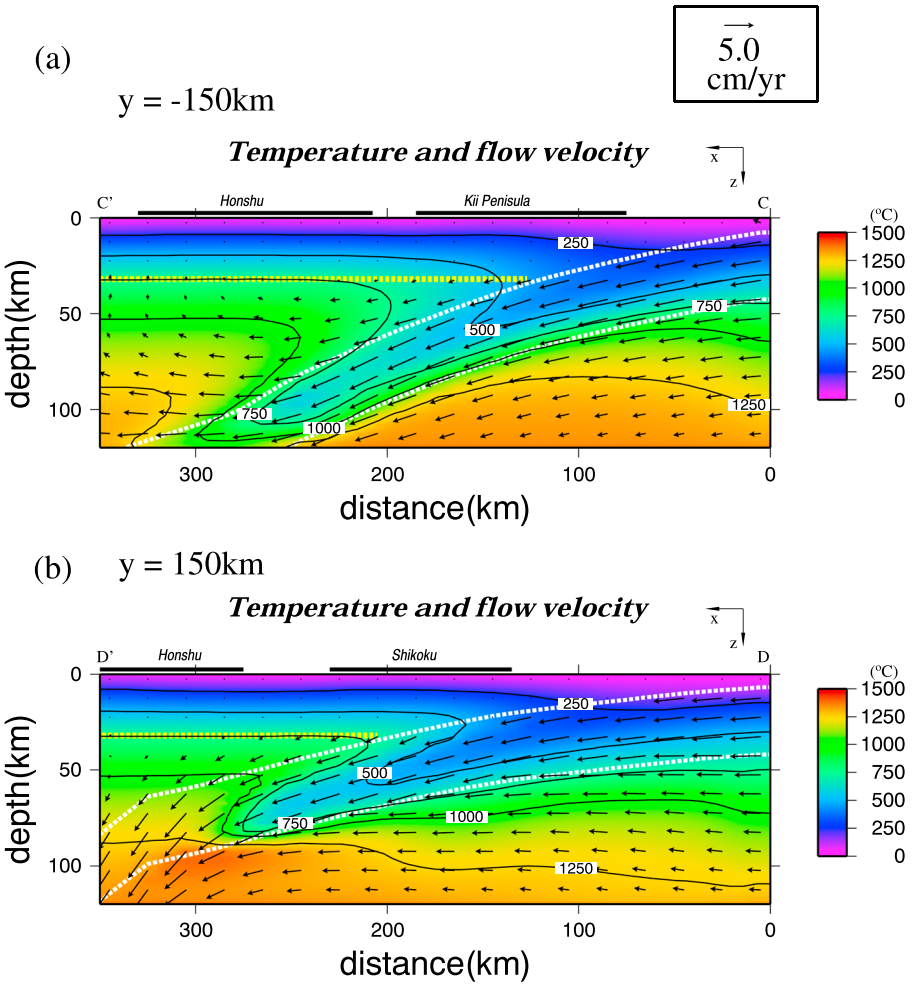

Figure 9. Distributions of temperature (color) and *x-z* component of mantle flow (black arrows) in the *x-z* vertical (trough normal) cross section at 0 Ma for Model 1. The two white dotted curves indicate the upper and lower surfaces of the subducting PHS plate. The yellow dotted line indicates the continental Moho discontinuity. (a) $y = -150$ km. (b) $y = 150$ km.

et al., 2013] in the Shikoku Basin, along with the trough-parallel distance from the FR with a thermal conductivity of 1.0 $Wm^{-1}K^{-1}$ at the seafloor, can decrease the observation of seafloor heat flow by nearly 30% (30–60 mW/m^2), whereas we assumed the thermal conductivity to be 1.5 $Wm^{-1}K^{-1}$ for the accretionary prism. For the remaining portion of the heat flow values along the Nankai Trough (Figure 5b), *Grose and Afonso* [2013] argued that the insulating property of the oceanic crust is a significant second-order contributor to the cooling behavior of oceanic lithosphere for young seafloor (<35 Ma), thus yielding differences between predicted values from the models and the observed surface heat flow.

5.2. Thermal Control of Megathrust Earthquakes

Hyndman et al. [1995] suggested that the updip and the downdip limits of the seismogenic zone on a plate interface in subduction zones are basically controlled by temperature. In this study, based on the complex geometry of the subducting PHS plate and its subduction history, a 3-D simulation provided more insights to better understand the thermal structure on the plate interface of the subducting PHS plate (Figure 10), which was constrained by a large amount of heat flow data (Figures 4 and 5). The updip limit of the seismogenic zone in the temperature range of 100–150°C advanced northward by ~50 km, mainly in the south of Shikoku, as compared with *Yoshioka and Murakami* [2007]. This is considered to be due to the introduction of the seafloor bathymetry into the model, which produced an assumed temperature of 0°C at a depth of approximately 5 km along the Nankai Trough, resulting in a deeper location (at approximately 15 km) for the calculated temperature contour of 150°C. The epicenters of the last two megathrust earthquakes

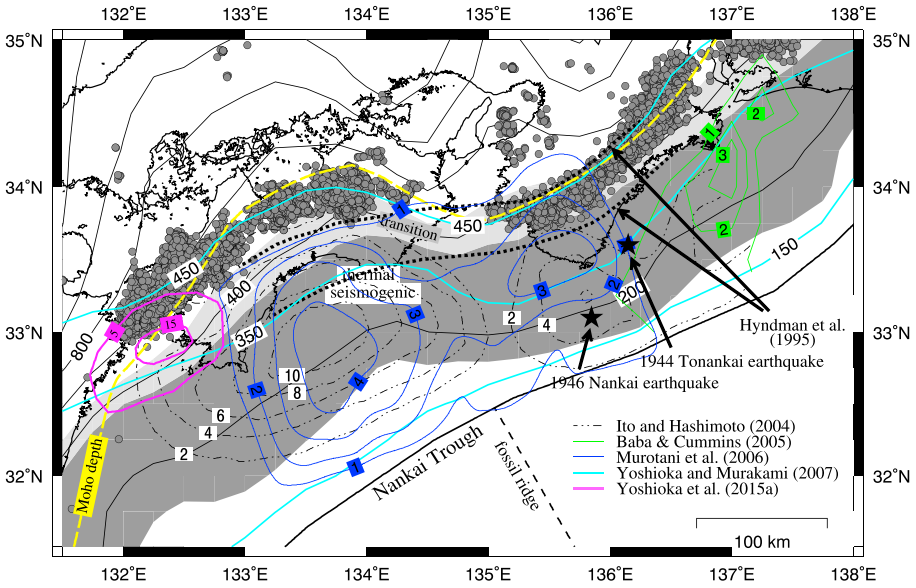

Figure 10. Interplate temperature distribution at 0 Ma for Model 1. The interplate temperature is divided into three regimes: 0–150°C, 150–350°C, and 350–450°C with different colors, corresponding to the shallow stable sliding zone (white), thermal seismogenic zone (dark gray), and transition zone (light gray), respectively, as compared with the interplate temperature estimated by the models of *Hyndman et al.* [1995] (two black dotted curves of 350°C and 450°C), and *Yoshioka and Murakami* [2007] (light blue curves). Epicenters of the 1944 Tonankai and 1946 Nankai earthquakes are shown with black solid stars. Coseismic slip distributions associated with the 1944 Tonankai and 1946 Nankai earthquakes obtained by inversion analyses of tsunami data [*Baba and Cummins*, 2005], seismic data [*Murotani et al.*, 2006], and geodetic data [*Ito and Hashimoto*, 2004] are shown. The unit of the contours is in meter. The small solid circles are epicenters of low-frequency earthquakes during the period from 1 October 1997 to 28 February 2015, which were taken from the unified hypocenter catalogue of low-frequency earthquakes of the Japan Meteorological Agency. The dashed yellow curve indicates the continental Moho depth on the plate interface. The two pink circled curves denote the area of the slow slip events beneath the Bungo Channel with slips of 5 cm (the outer ellipse) and 15 cm (the inner ellipse) during the 2010 long-term slow slip events (L-SSEs) obtained by *Yoshioka et al.* [2015a].

(1944 Tonankai and 1946 Nankai) were also located in the thermally estimated seismogenic zone off the Kii Peninsula, and large coseismically slipped regions associated with the two earthquakes were obtained by inversion analyses of tsunami data [*Baba and Cummins*, 2005], seismic data [*Murotani et al.*, 2006], and geodetic data [*Ito and Hashimoto*, 2004]. The updip limit of the seismogenic zone reached a depth of 10 km [e.g., *Saffer and Marone*, 2003; *Yoshioka et al.*, 2015b], which indicates that the temperature was in a transition from below 100–150°C to a higher value, corresponding to a possible dehydration process from smectite to illite. Considering the consistency between the observed and calculated surface heat flow, a more reliable estimated interplate temperature was obtained, taking account of the plate geometry, subduction history, obliquity of subduction, and bathymetry correction to calculate the surface heat flow.

5.3. Thermal Control of Nonvolcanic Deep Low-Frequency Earthquakes and Long-Term Slow Slip Events

We also plotted the foci of nonvolcanic low-frequency earthquakes (LFEs) that occurred in southwest Japan during a period from 1 October 1997 to 28 February 2015, which were taken from the JMA (Japan Meteorological Agency) unified hypocenter catalogue (Figure 10). Comparing with *Hyndman et al.* [1995], the transition zone of 350–450°C also moved northward by tens of kilometers in Shikoku, but generally maintained its features. Comparing the temperature distribution on the plate interface with the epicenters of nonvolcanic deep LFEs in southwest Japan, we found that the epicenters of LFEs were distributed with a temperature range from approximately 400 to 700°C in southwest Japan and from 450 to 700°C in western Shikoku. *Yoshioka and Murakami* [2007] proposed that the temperature range for LFEs ranges from 400 to 500°C. According to the phase diagram of the mid-ocean ridge basalt (MORB) proposed by *Hacker et al.* [2003] and *Omori et al.* [2009], we suggest that most of the LFEs that occurred within this temperature range were presumably related to the blueschist-amphibolite or lawsonite-amphibolite phase transformation of the hydrous minerals in the MORB of the oceanic crust of the subducting PHS plate.

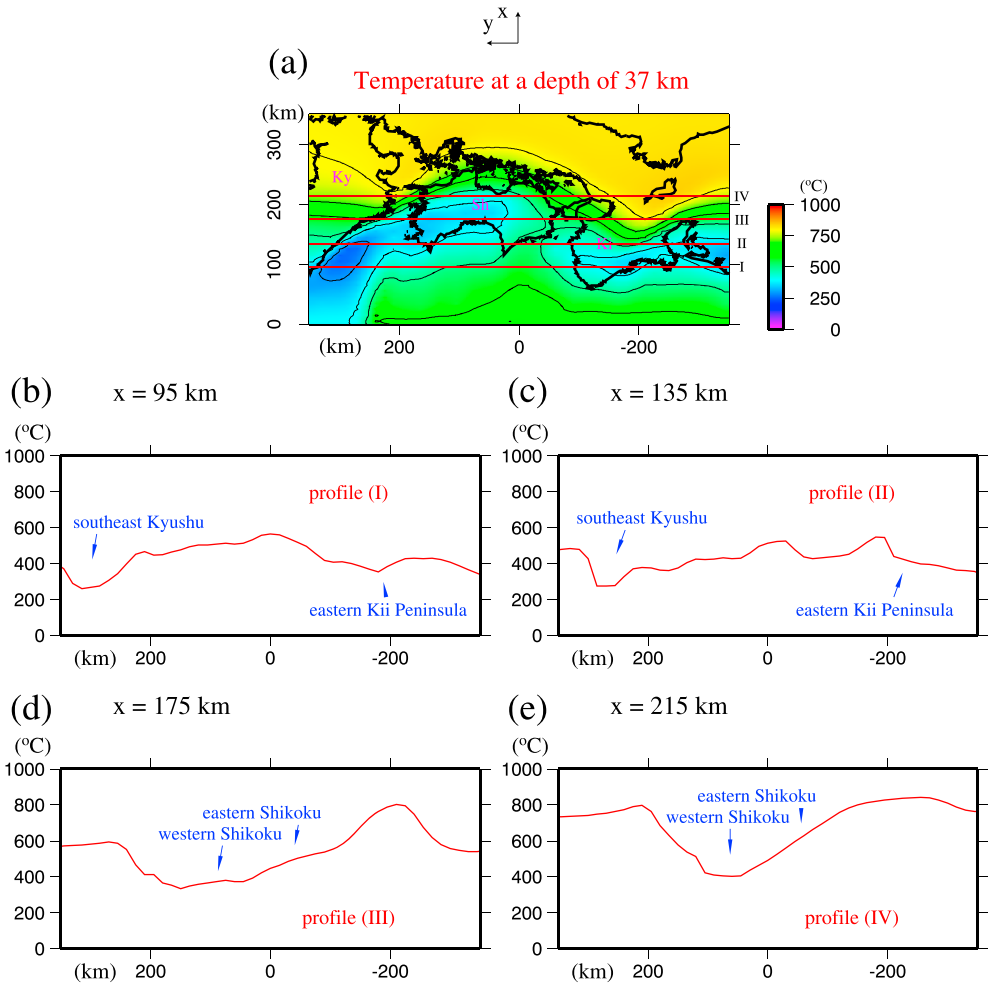

Figure 11. (a) Calculated temperature distribution at a depth of 37 km at 0 Ma for Model 1. The red lines indicate the locations of profiles I to IV whose temperatures are shown in Figures 11b–11e, respectively. Ky: Kyushu, Sh: Shikoku, Ki: Kii Peninsula. (b) Calculated temperature along profile I ($x = 95$ km) in Figure 11a in the y direction. (c) Same as Figure 11b but along profile II ($x = 135$ km). (d) Same as Figure 11b but along profile III ($x = 175$ km). (e) Same as Figure 11b but along profile IV ($x = 215$ km).

The temperature distribution at a depth of 37 km is shown in Figure 11a as well as the temperatures along four profiles, which are almost parallel to the Nankai Trough from $x = 95$ to 215 km (Figures 11b–11e). This depth is close to the base of the continental Moho and within the range of 35–45 km where the nonvolcanic LFEs are speculated to occur [*Nakamura et al.*, 1997]. Distinct low temperature can be seen (Figure 11a) on the descent slope of the slab surface in the convergent direction, where there were larger subduction angles, such as beneath southeast Kyushu (Figures 11b and 11c), western Shikoku (Figures 11d and 11e), and the eastern Kii Peninsula (Figures 11b and 11c). These features were also found for temperature distributions at the depths of 43 km and 63 km (Figures 7a and 7b). This similarity among different depths indicates that the PHS plate has a similar thermal structure associated with subduction deep into the uppermost mantle. Furthermore, Figure 11e shows that slab core temperature in western Shikoku can be 200°C lower than that in eastern Shikoku near the base of the continental Moho.

The temperature distribution at a depth of 37 km and the foci of LFEs at depths of 28–38 km are shown in Figure 12. The red curve in Figure 12b shows the temperature along the upper surface of the PHS plate at a depth of 37 km along the plate interface (orange curve U) in Figure 12a. The blue curve in Figure 12b indicates the horizontal temperature gradient along the landward direction (x direction) at this depth, which was obtained from the temperature difference between the grids on the plate interface (orange curve U in Figure 12a) and the grids 20 km horizontally troughward inside the slab.

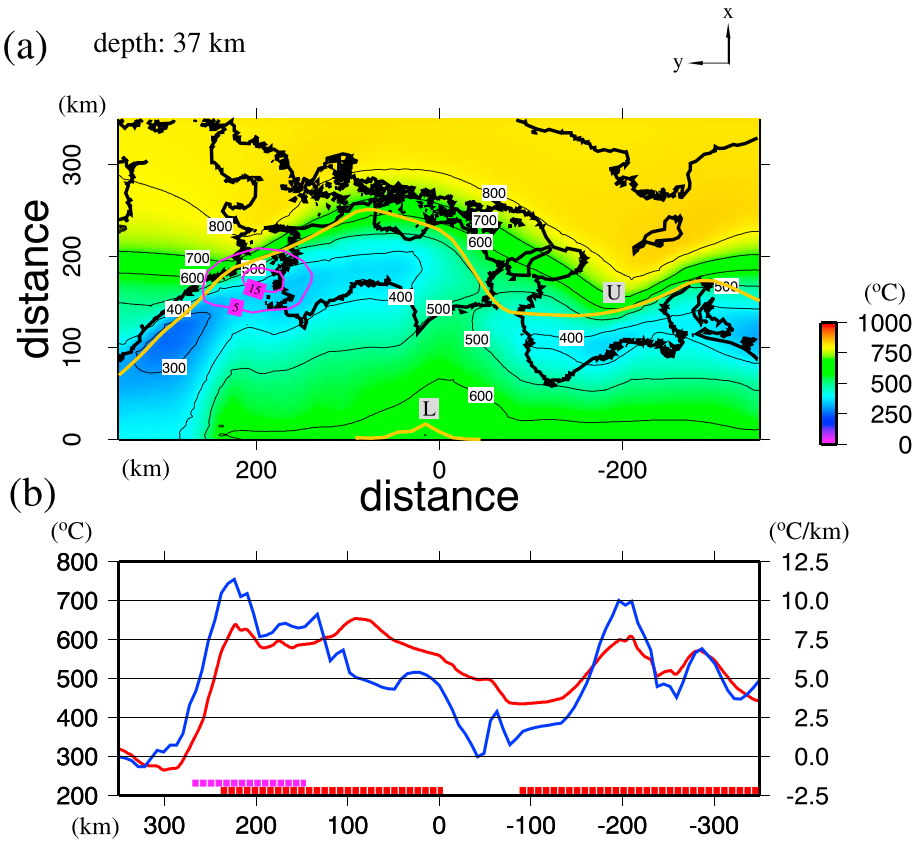

Figure 12. (a) Calculated temperature distribution at a depth of 37 km at 0 Ma for Model 1. The red circles indicate the foci of low-frequency earthquakes at depths ranging from 28 to 38 km that occurred in southwest Japan from 1 October 1997 to 28 February 2015. The purple curve indicates the slip distribution of a typical L-SSE from May 2009 to February 2011 [*Yoshioka et al.*, 2015a]. The orange curve indicates the upper and lower surfaces of the PHS plate. U: upper surface of the PHS slab; L: lower surface of the PHS slab. (b) The red curve is temperature along the upper surface of the PHS plate at a depth of 37 km (along the orange curve U in Figure 12a). The blue curve indicates the temperature gradient along the horizontal trough-perpendicular landward direction at a depth of 37 km, which was calculated from the temperature difference between the grids at the plate interface (orange curve U) and the corresponding grids 20 km horizontally troughward from the plate interface. The horizontal axis (distance) in Figure 12b is projected from the horizontal axis (distance) in Figure 12a. On the bottom of Figure 12b, a thick dashed purple bar indicates the location where L-SSEs occurred, and the thick dashed red bar indicates the location where LFEs occurred.

In Figure 12a, it can be seen that the distribution of the deep LFEs beneath southwest Japan exhibits some coincidence with the iso-depth contours of the upper surface of the PHS plate. However, we noticed a lack of deep LFEs in eastern Shikoku, indicating that the distribution of the deep LFEs was probably controlled not only by the depth (pressure) but also by the temperature because a warmer region existed in both the slab core and plate interface beneath eastern Shikoku. Figures 12a and 12b show that the clustering of foci of the deep LFEs occurred at a temperature range of 400–700°C. The horizontal temperature gradient (Figure 12b) adjacent to the plate interface had a high value of 2.5 ~°C/km at western Shikoku and the eastern Kii Peninsula. This may be interpreted as the thermal effect of the distribution of LFEs in this region. The gap in the LFE distribution beneath eastern Shikoku had a lower horizontal thermal gradient adjacent to the plate interface with a value less than 2.5°C/km in the numerical simulation.

More interestingly, according to the slip distribution of a typical long-term slow slip event (L-SSE) during the period from May 2009 to February 2011 (circled by the purple curve in Figure 12a [*Yoshioka et al.*, 2015a]) with the temperatures shown in Figures 11 and 12, L-SSEs occurred beneath the Bungo Channel, where a larger horizontal temperature gradient (>5.0°C/km) was apparent (part of the blue curve with values greater than 5.0°C/km in Figure 12b). The updip and downdip limits of the temperatures for the L-SSE for a slip of >15 cm ranged from approximately 350 to 500°C at the center for most slips (Figure 10). The larger horizontal

temperature gradient, with a peak value of over 5.0°C/km beneath the Bungo Channel, was expected to yield regional variation in dehydration and serpentinization near the plate interface. From the phase diagram of MORB [*Hacker et al.*, 2003], we estimated the depth of the plate interface to be almost 25 km, corresponding to the dehydration process from lawsonite or blueschist to amphibolite.

Shiomi et al. [2008] proposed that active regions of intraslab regular earthquakes correspond well to the oceanic Moho geometry. They attributed the fewer regular earthquakes in eastern Shikoku to the strike-slip focal mechanism and its extension axes being parallel to the strike of the oceanic Moho, which contrasts to the downdip compression focal mechanism in western Shikoku. However, from another perspective, the geometry of an oceanic plate also influences the thermal regime of the slab. We propose to interpret this kind of heterogeneity based on the relationships among the subduction angle, interplate temperature, and phase transformation of hydrous minerals, which were estimated by the numerical simulation. We noticed that LFEs are assembled on the cold side of the slab geometry with a larger subduction angle such as western Shikoku, the Bungo Channel, and the Kii Peninsula. LFEs occurred near the depth of the continental Moho and have hypocenters that coincide with the thermal range of approximately 350–700°C beneath southwest Japan. L-SSEs occurred mostly beneath the Bungo Channel, which is a steeper side of the slab geometry with a larger subduction angle and higher horizontal temperature gradient appearing simultaneously. This may facilitate slab dehydration, and thus elevate pore fluid pressure and water content in the subducted slab and mantle wedge near the plate interface, relating the fault slip and slow earthquakes [e.g., *Chernak and Hirth*, 2011; *Ikari et al.*, 2013].

6. Conclusions

The PHS plate is subducting beneath the Eurasian plate (15–3 Ma) and the Amurian plate (3–0 Ma) beneath southwest Japan, forming complex temperature and mantle flow fields near the upper surface of the slab. Using a 3-D parallelepiped model of the subducting plate in the thermal convection, we investigated the spatiotemporal features of the distributions of temperature and mantle flow associated with subduction of the PHS plate. The main results of this study can be summarized as follows:

1. The age of the subducting plate, frictional heating on the plate interface, and radioactive heat generation were the key parameters that constrained the model to fit the observed heat flow. Bathymetry also contributed to the distribution of the surface heat flow in the ocean.
2. The effect of the 3-D geometry of the subducting plate and the obliquity of plate subduction were the key factors that affected the interplate and intraslab temperatures, resulting in a colder anomaly on the plate interface beneath western Shikoku, the Bungo Channel, and the Kii Peninsula. The temperatures in such areas were lower by nearly 200°C in the slab core than that in eastern Shikoku at the depth of the continental Moho. This yielded remarkable lateral heterogeneity in the interplate thermal regime of the PHS plate.
3. LFEs were distributed along the interplate downdip fault zone, where a larger subduction angle and a cold thermal anomaly existed. Thermal control for the LFEs was estimated to be within the range from 350 to 700°C beneath southwest Japan and from 400 to 700°C beneath western Shikoku. The horizontal temperature gradient attributable to the occurrence of the LFEs was considered to be larger than 2.5°C/km beneath western Shikoku and the Kii Peninsula.
4. The interplate thermal control for the L-SSEs beneath the Bungo Channel was estimated to be approximately 350–500°C for slips larger than 15 cm. A horizontal temperature gradient greater than 5.0°C/km was present where the L-SSEs occurred repeatedly. Large temperature gradient may facilitate slab dehydration and the phase transformation of hydrous minerals from lawsonite or blueschist to amphibolite within the MORB of the subducted oceanic crust.

Acknowledgments

We thank Paul Tackley for sharing the original source code of stag3D for our numerical simulation. We also thank Fuyuki Hirose, Junichi Nakajima, Ayako Nakanishi, Shuichi Kodaira, and Dapeng Zhao for providing us with the geometry data of the upper surface of the subducting Philippine Sea plate beneath southwest Japan. The JMA hypocenter catalogue of low-frequency earthquakes was used in this study. We also thank Satoru Honda and an anonymous reviewer for their constructive comments. This work was partly supported by MEXT KAKENHI grant 21107007 and JSPS KAKENHI grant JP16H04040. All the figures were created by the Generic Mapping Tools developed by *Wessel and Smith* [1998] and Paraview software developed by Kitware Inc. The data for this paper are available by contacting the corresponding author at 31911431@qq.com.

References

Argus, D. F., R. G. Gordon, and C. DeMets (2011), Geologically current motion of 56 plates relative to the no-net-rotation reference frame, *Geochem. Geophys. Geosyst.*, *12*, Q11001, doi:10.1029/2011GC003751.

Ashi, J., H. Tokuyama, Y. Ujiie, and A. Taira (1999), Heat flow estimation from gas hydrate BSRs in the Nankai Trough: Implications for the thermal structures of the Shikoku Basin, *Eos Trans. AGU*, *80*(46), Suppl. T12A-02.

Ashi, J., H. Tokuyama, and A. Taira (2002), Distribution of methane hydrate BSRs and its implication or the prism growth in the Nankai Trough, *Mar. Geol.*, *187*, 117–191.

Baba, T., and P. R. Cummins (2005), Contiguous rupture areas of two Nankai earthquakes revealed by high-resolution tsunami waveform inversion, *Geophys. Res. Lett.*, *32*, L08305, doi:10.1029/2004GL022320.
Burkett, E. R., and M. I. Billen (2010), Three-dimensionality of slab detachment due to ridge-trench collision: Laterally simultaneous boudinage versus tear propagation, *Geochem. Geophys. Geosyst.*, *11*, Q11012, doi:10.1029/2010GC003286.
Byerlee, J. D. (1978), Friction of rocks, *Pure Appl. Geophys.*, *116*, 615–626.
Capitanio, F. A., and G. Morra (2012), The bending mechanics in a dynamic subduction system: Constraints from numerical modeling and global compilation, *Tectonophysics*, *522–523*, 224–234.
Capitanio, F. A., G. Morra, and S. Goes (2009), Dynamics of plate bending at the trench and slab-plate coupling, *Geochem. Geophys. Geosyst.*, *10*, Q04002, doi:10.1029/2008GC002348.
Caristan, Y. (1982), The transition from high temperature creep to fracture in maryland diabase, *J. Geophys. Res.*, *87*, 6781–6790, doi:10.1029/JB087iB08p06781.
Chernak, L., and G. Hirth (2011), Syndeformational antigorite dehydration produces stable fault slip, *Geology*, *39*, 847–850.
Christensen, U. R. (1996), The influence of trench migration on slab penetration into the lower mantle, *Earth Planet. Sci. Lett.*, *140*, 27–39.
Clift, P. D., A. Carter, U. Nicholson, and H. Masago (2013), Zircon and apatite thermochronology of the Nankai Trough accretionary prism and trench, Japan: Sediment transport in an active and collisional margin setting, *Tectonics*, *32*, 377–395, doi:10.1002/tect.20033.
DeMets, C., R. G. Gordon, and D. F. Argus (2010), Geologically current plate motions, *Geophys. J. Int.*, *181*(1), 1–80, doi:10.1111/j.1365-246X.2009.04491.x.
Di Giuseppe, E., J. van Hunen, F. Funiciello, C. Faccenna, and D. Giardini (2008), Slab stiffness control of trench motion: Insights from numericalmodels, *Geochem. Geophys. Geosyst.*, *9*, Q02014, doi:10.1029/2007GC001776.
Fukahata, Y., and M. Matsu'ura (2000), Effects of active crustal movements on thermal structure in subduction zones, *Geophys. J. Int.*, *141*, 271–281.
Funiciello, F., G. Morra, K. Regenauer-Lieb, and D. Giardini (2003), Dynamics of retreating slabs: 1. Insights from two-dimensional numerical experiments, *J. Geophys. Res.*, *108*(B4), 2206, doi:10.1029/2001JB000898.
Funiciello, F., C. Faccenna, A. Heuret, S. Lallemand, E. Di Giuseppe, and T. W. Becker (2008), Trench migration, net rotation and slab-mantle coupling, *Earth Planet. Sci. Lett.*, *271*, 233–240.
Furukawa, Y. (1999), Interplate coupling and deformation in the accretionary prism in the Southwest Japan Subduction Zone, *Geophys. Res. Lett.*, *26*, 3145–3148, doi:10.1029/1999GL005403.
Gao, X., and K. Wang (2014), Strength of stick-slip and creeping subduction megathrusts from heat flow observations, *Science*, *345*, 1038, doi:10.1126/science.1255487.
Gerya, T. (2011), Future directions in subduction modeling, *J. Geodyn.*, *5*, 344–378.
Goes, S., F. A. Capitanio, and G. Morra (2008), Evidence of lower-mantle slab penetration phases in plate motions, *Nature*, *451*, 981–984, doi:10.1038/nature06691.
Gorbatov, A., and V. Kostoglodov (1997), Maximum depth of seismicity and thermal parameter of the subducting slab: General empirical relation and its application, *Tectonophysics*, *277*, 165–187.
Grose, C. J., and J. C. Afonso (2013), Comprehensive plate models for the thermal evolution of oceanic lithosphere, *Geochem. Geophys. Geosyst.*, *14*, 3751–3778, doi:10.1002/ggge.20232.
Hacker, B. R., G. A. Abers, and S. M. Peacock (2003), Subduction factory 1. Theoretical mineralogy, densities, seismic wave speeds, and H_2O contents, *J. Geophys. Res.*, *108*(B1), 2029, doi:10.1029/2001JB001127.
Hamamoto, H., M. Yamano, S. Goto, M. Kinoshita, K. Fujino, and K. Wang (2011), Heat flow distribution and thermal structure of the Nankai subduction zone off the Kii Peninsula, *Geochem. Geophys. Geosyst.*, *12*, Q0AD20, doi:10.1029/2011GC003623.
Hansen, F. D., and N. L. Carter (1983), Semibrittle creep of dry and wet Westerly granite at 1000 MPa, in *U.S. Symposium on Rock Mechanics*, vol. 24, pp. 429–447, Tex. A & M. Univ., College Station, Tex.
Harris, R., M. Yamano, M. Kinoshita, G. Spinelli, H. Hamamoto, and J. Ashi (2013), A synthesis of heat flow determinations and thermal modeling along the Nankai Trough, Japan, *J. Geophys. Res. Solid Earth*, *118*, 2687–2702, doi:10.1002/jgrb.50230.
Hirose, F., J. Nakajima, and A. Hasegawa (2008), Three-dimensional seismic velocity structure and configuration of the Philippine Sea slab in southwestern Japan estimated by double-difference tomography, *J. Geophys. Res.*, *113*, B09315, doi:10.1029/2007JB005274.
Hirth, G., and D. Kohlstedt (2003), Rheology of the upper mantle and the mantle wedge: A view from the experimentalists, in *Inside the Subduction Factory*, *Geophys. Monogr. Ser.*, vol. 138, edited by J. Eiler, pp. 83–105, AGU, Washington, D. C.
Honda, S. (2008), A simple semi-dynamic model of the subduction zone: Effects of a moving plate boundary on the small-scale convection under the island arc, *Geophys. J. Int.*, *173*, 1095–1105.
Honda, S., and M. Saito (2003), Small-scale convection under the back-arc occurring in the low viscosity wedge, *Earth Planet. Sci. Lett.*, *216*, 703–715.
Honda, S., and T. Yoshida (2005), Effects of oblique subduction on the 3-D pattern of small-scale convection within the mantle wedge, *Geophys. Res. Lett.*, *32*, L13307, doi:10.1029/2005GL023106.
Hyndman, R. D., K. Wang, and M. Yamano (1995), Thermal constraints on the seismogenic portion of the southwestern Japan subduction thrust, *J. Geophys. Res.*, *100*, 15,373–15,392, doi:10.1029/95JB00153.
Ikari, M. J., C. Marone, D. M. Saffer, and A. J. Kopf (2013), Slip weakening as a mechanism for slow Earthquakes, *Nat. Geosci.*, *6*, 468–472.
Ito, T., and M. Hashimoto (2004), Spatio-temporal distribution of interplate coupling in southwest Japan deduced from inversion analysis, *J. Geophys. Res.*, *109*, B02315, doi:10.1029/2002JB002358.
Iwamori, H. (1997), Heat sources and melting in subduction zones, *J. Geophys. Res.*, *102*, 14,803–14,820, doi:10.1029/97JB01036.
Jadamec, M. A., and M. I. Billen (2010), Reconciling surface plate motions with rapid three-dimensional mantle flow around a slab edge, *Nature*, *465*, 338–341, doi:10.1038/nature09053.
Ji, Y., and S. Yoshioka (2015), Effects of slab geometry and obliquity on the interplate thermal regime associated with the subduction of three-dimensionally curved oceanic plates, *Geosci. Front.*, *6*, 61–78.
Kimura, J., J. Robert, and T. Yoshida (2005), Reinitiation of subduction and magmatic responses in SW Japan during Neogene time, *Geol. Soc. Am. Bull.*, *117*, 969–986.
Kneller, E. A., and P. E. van Keken (2008), Effect of three-dimensional slab geometry on deformation in the mantle wedge: Implications for shear wave anisotropy, *Geochem. Geophys. Geosyst.*, *9*, Q01003, doi:10.1029/2007GC001677.
Lassak, T. M., M. J. Fouch, C. E. Hall, and E. Kaminski (2006), Seismic characterization of mantle flow in subduction systems: Can we resolve a hydrated mantle wedge?, *Earth Planet. Sci. Lett.*, *243*, 632–649.
Li, Z. H., and N. M. Ribe (2012), Dynamics of free subduction from 3D boundary element modeling, *J. Geophys. Res.*, *117*, B06408, doi:10.1029/2012JB009165.

Long, M. D., and P. G. Silver (2008), The subduction zone flow field from seismic anisotropy: A global view, *Science*, *319*, 315–318, doi:10.1126/science.1150809.
Mahony, S. H., L. M. Wallace, M. Miyoshi, P. Villamor, R. S. J. Sparks, and T. Hasenaka (2011), Volcano-tectonic interactions during rapid plate-boundary evolution in the Kyushu region, SW Japan, *Geol. Soc. Am. Bull.*, *123*, 2201–2223, doi:10.1130/B30408.1.
Manea, V. C., M. P. Gussinyé, and M. Manea (2012), Chilean flat slab subduction controlled by overriding plate thickness, and trench rollback, *Geology*, *1*, 35–38.
Matsumoto, T. (2007), Terrestrial heat flow distribution in Japan area based on the temperature logging in the borehole of NIED Hi-net, Abstract T23A-1217 presented at 2007 Fall Meeting, AGU.
McKenzie, D. P. (1967), Some remarks on heat flow and gravity anomalies, *J. Geophys. Res.*, *72*, 6261–6273, doi:10.1029/JZ072i024p06261.
Morishige, M., and P. E. van Keken (2014), Along-arc variation in the 3-D thermal structure around the junction between the Japan and Kurile arcs, *Geochem. Geophys. Geosyst.*, *15*, 2225–2240, doi:10.1002/2014GC005394.
Morishige, M., S. Honda, and P. J. Tackley (2010), Construction of semi-dynamic model of subduction zone with given plate kinematics in 3D sphere, *Earth Planets Space*, *62*, 665–673.
Morra, G., K. Regenauer-Lieb, and D. Giardini (2006), Curvature of oceanic arcs, *Geology*, *34*, 877–880.
Morra, G., P. Chatelain, P. J. Tackley, and P. Koumoutsakos (2009), Earth curvature effects on subduction morphology: Modeling subduction in a spherical setting, *Acta Geotech.*, *4*, 95–105.
Murotani, S., K. Shimazaki, K. Koketsu, T. Furumura, T. Baba, and P. Cummins (2006), Source process of the 1946 Nankai earthquake estimated from inversion of teleseismic waveforms, Abstract S117–001presented at Japan Geoscience Union Meeting.
Nakajima, J., and A. Hasegawa (2007), Subduction of the Philippine Sea plate beneath southwestern Japan: Slab geometry and its relationship to arc magmatism, *J. Geophys. Res.*, *112*, B08306, doi:10.1029/2006JB004770.
Nakamura, M., H. Watanabe, T. Konomi, S. Kimura, and K. Miura (1997), Characteristic activities of subcrustal earthquakes along the outer zone of southwestern Japan [in Japanese with English abstract], *Ann. Disaster Prev. Res. Inst., Kyoto Univ.*, *40*(B-1), 1–20.
Nakanishi, A., N. Shimomura, S. Kodaira, K. Obana, T. Takahashi, Y. Yamamoto, M. Yamashita, N. Takahashi, and Y. Kaneda (2012), Three-dimensional model of plate geometry and velocity model for Nankai Trough seismogenic zone based on results from structural studies, Abstract T13C-2616 presented at AGU Fall meeting 2012.
Obara, K., and H. Hirose (2006), Non-volcanic deep low-frequency tremors accompanying slow slips in the southwest Japan subduction zone, *Tectonophysics*, *417*, 33–51.
Okino, K., Y. Ohara, S. Kasuga, and Y. Kato (1999), The Philippine Sea: New survey results reveal the structure and the history of the marginal basins, *Geophys. Res. Lett.*, *26*, 2287–2290, doi:10.1029/1999GL900537.
Omori, S., S. Kita, S. Maruyama, and M. Santosh (2009), Pressure-temperature conditions of ongoing regional metamorphism beneath the Japanese Islands, *Gondwana Res.*, *16*, 458–469.
OzBench, M., et al. (2008), A model comparison study of large-scale mantle-lithosphere dynamics driven by subduction, *Phys. Earth Planet. Inter.*, *171*, 224–234.
Ranalli, G. (1995), *Rheology of the Earth*, 2nd ed., 76 pp., Chapman and Hall, London.
Saffer, D. M., and C. Marone (2003), Comparison of smectite- and illiterich gouge frictional properties: Application to the updip limit of the seismogenic zone along subduction megathrusts, *Earth Planet. Sci. Lett.*, *215*, 219–235.
Schellart, W. P., J. Freeman, D. R. Stegman, L. Moresi, and D. May (2007), Evolution and diversity of subduction zones controlled by slab width, *Nature*, *446*, 308–311.
Schmeling, H., et al. (2008), A benchmark comparison of spontaneous subduction models—Towards a free surface, *Phys. Earth Planet. Inter.*, *171*, 198–223.
Sella, G. F., T. H. Dixon, and A. Mao (2002), REVEL: A model for Recent plate velocities from space geodesy, *J. Geophys. Res. 107*(B4), 2081, doi:10.1029/2000JB000033.
Seno, T. (2009), Determination of the pore fluid pressure ratio at seismogenic megathrusts in subduction zones: Implications for strength of asperities and Andean-type mountain building, *J. Geophys. Res.*, *114*, B05405, doi:10.1029/2008JB005889.
Shiomi, K., M. Matsubara, Y. Ito, and K. Obara (2008), Simple relationship between seismic activity along Philippine Sea slab and geometry of oceanic Moho beneath southwest Japan, *Geophys. J. Int.*, *173*, 1018–1029.
Spinelli, G. A., and K. Wang (2008), Effects of fluid circulation in subducting crust on Nankai margin seismogenic zone temperatures, *Geology*, *36*(11), 887–890.
Stegman, D. R., J. Freeman, W. P. Schellart, L. Moresi, and D. May (2006), Influence of trench width on subduction hinge retreat rates in 3-D models of slab rollback, *Geochem. Geophys. Geosyst.*, *7*, Q03012, doi:10.1029/2005GC001056.
Stegman, D. R., R. Farrington, F. A. Capitanio, and W. P. Schellart (2010a), A regime diagram for subduction styles from 3-D numerical models of free subduction, *Tectonophysics*, *483*, 29–45.
Stegman, D. R., W. P. Schellart, and J. Freeman (2010b), Competing influences of plate width and far-field boundary conditions on trenchmigration andmorphology of subducted slabs in the upper mantle, *Tectonophysics*, *483*, 46–57.
Stein, C. A., and S. Stein (1992), A model for the global variation in oceanic depth and heat flow with lithospheric age, *Nature*, *359*, 123–129.
Strak, V., and W. P. Schellart (2014), Evolution of 3-D subduction-induced mantle flow around lateral slab edges in analogue models of free subduction analysed by stereoscopic particle image velocimetry technique, *Earth Planet. Sci. Lett.*, *403*, 368–379.
Tackley, P. J. (1998), Self-consistent generation of tectonic plates in threedimensional mantle convection, *Earth Planet. Sci. Lett.*, *157*, 9–22.
Tackley, P. J. (2000), Self-consistent generation of tectonic plates in time-dependent, three-dimensional mantle convection simulations. Part 1: Pseudo-plastic yielding, *Geochem. Geophys. Geosyst.*, *1*(1), 1021, doi:10.1029/2000GC000036.
Tackley, P. J., and S. Xie (2003), Stag3D: A code for modeling thermo-chemical multiphase convection, in *Proceedings of the Second MIT Conference on Computational Fluid and Solid Mechanics*, edited by K. J. Bathe, pp. 1524–1527, Elsevier B.V., Amsterdam.
Takahashi, M. (2006), Tectonic development of the Japanese Islands controlled by Philippine Sea plate motion, *J. Geogr.*, *115*, 116–123.
Tanaka, A., M. Yamano, Y. Yano, and M. Sasada (2004), Geothermal gradient and heat flow data in and around Japan, digital geoscience map, DGMP-5, Geol. Surv. of Jpn.
The Headquarters for Earthquake Research Promotion (2004), On long-term evaluation of seismic activity in and around the Hyuganada and Nansei islands trench [in Japanese]. [Available at http://www.jishin.go.jp/main/chousa/kaikou_pdf/hyuganada.pdf.]
The Research Group for the Quaternary Tectonic Map (1969), Explanatory text of the Quaternary tectonic map of Japan 1-7 [in Japanese], NIED Disaster Inf. Lab., Tsukuba.
Tokuyama, H. (1995), Origin and development of the Philippine Sea, in *Geology and Geophysics of the Philippine Sea*, edited by H. Tokuyama et al., pp. 155–163, Terrapub, Tokyo.
Turcotte, D. L., and G. Schubert (2002), *Geodynamics*, 2nd ed., 186 pp., Cambridge Univ. Press, Cambridge, U. K.

Uehara, D., T. Ishimaru, A. Tanase, Y. Ogawa, and T. Kagiyama (2003), Effectiveness of far remote reference method on magnetotelluric (MT) survey and deep resistivity structure in the southern region of the Kii Peninsula, Southwest Japan [in Japanese], *J. Jpn. Soc. Eng. Geol.*, *44*(3), 164–174.

van Keken, P. E., et al. (2008), A community benchmark for subduction zone modeling, *Phys. Earth Planet. Inter.*, *171*, 187–197.

Völker, D., I. Grevemeyer, M. Stipp, K. Wang, and J. He (2011), Thermal control of the seismogenic zone of southern central Chile, *J. Geophys. Res.*, *116*, B10305, doi:10.1029/2011JB008247.

Wada, I., and K. Wang (2009), Common depth of slab-mantle decoupling: Reconciling diversity and uniformity of subduction zones, *Geochem. Geophys. Geosyst.*, *10*, Q10009, doi:10.1029/2009GC002570.

Wada, I., J. He, A. Hasegawa, and J. Nakajima (2015), Mantle wedge flow pattern and thermal structure in Northeast Japan: Effects of oblique subduction and 3-D slab geometry, *Earth Planet. Sci. Lett.*, *426*, 76–88.

Wang, K., R. D. Hyndman, and M. Yamano (1995), Thermal regime of the Southwest Japan subduction zone: Effects of age history of the subducting plate, *Tectonophysics*, *248*, 53–69.

Wessel, P., and W. H. F. Smith (1998), New, improved version of the generic mapping tools released, *Eos Trans. AGU*, *79*, 579, doi:10.1029/98EO00426.

Yoshida, M., F. Tajima, S. Honda, and M. Morishige (2012), The 3D numerical modeling of subduction dynamics: Plate stagnation and segmentation, and crustal advection in the wet mantle transition zone, *J. Geophys. Res.*, *117*, B04104, doi:10.1029/2011JB008989.

Yoshii, T. (1975), Regionality of group velocities of Rayleigh waves in the Pacific and thickening of the plate*t*, *Earth Planet. Sci. Lett.*, *25*, 305–312.

Yoshikawa, T. (1974), Denudation and tectonic movement in contemporary Japan, *Bull. Dep. Geogr. Univ. Tokyo*, *6*, 1–14.

Yoshioka, S., and K. Murakami (2007), Temperature distribution of the upper surface of the subducted Philippine Sea plate, southwest Japan, from a three-dimensional subduction model: Relation to largeinterplate and low-frequency earthquakes, *Geophys. J. Int.*, *171*, 302–315.

Yoshioka, S., Y. Suminokura, T. Matsumoto, and J. Nakajima (2013), Two-dimensional thermal modeling of subduction of the Philippine Sea plate beneath southwest Japan, *Tectonophysics*, *608*, 1094–1108.

Yoshioka, S., Y. Matsuoka, and S. Ide (2015a), Spatiotemporal slip distributions of three long-term slow slip events beneath the Bungo Channel, southwest Japan, inferred from inversion analyses of GPS data, *Geophys. J. Int.*, *201*, 1437–1455.

Yoshioka, S., R. Takagi, and T. Matsumoto (2015b), Relationship between temperatures and fault slips on the upper surface of the subducting Philippine Sea Plate beneath the Kanto district, central Japan, *Geophys. J. Int.*, *201*, 878–890.

Zhao, D., T. Yanada, A. Hasegawa, N. Umino, and W. Wei (2012), Imaging the subducting slabs and mantle upwelling under the Japan Islands, *Geophys. J. Int.*, *190*, 816–828.

Zhu, G., Y. Shi, and P. J. Tackley (2010), Subduction of the Western Pacific Plate underneath Northeast China: Implications of numerical studies, *Phys. Earth Planet. Inter.*, *178*, 92–99.